adequately assess adverse health risks to children, the inhalation rate of young children in daily life needs to be determined.

The doubly labeled water (DLW) method and the time-activity-ventilation method are experimental approaches that have been used to estimate daily inhalation rates during the daily activities of free-living individuals.[5–11] The DLW method is the most accurate method to measure the average total energy expenditure (EE) of people over several days and is based on the rates of disappearance of a dose of water containing the stable isotopes ^2H and ^{18}O. Although the DLW approach provides an accurate estimation of the daily inhalation rate, it is an expensive method and requires the collection of urine samples for 2–3 weeks. By comparison, the time-activity-ventilation method estimates the volume of air inhaled by a person over a defined period of time as a time-weighted average of the minute ventilation rate (V_E) for each level of activity during the period. The daily inhalation rate using this approach is expressed by the following equation:

$$\text{Daily inhalation rate} = \left[\sum_{i=1}^{k} \dot{V}_{Ei} \times t_i \right] \times 10^{-3} \quad (1)$$

where *Daily inhalation rate* is the 24-hr inhalation rate ($m^3 \cdot day^{-1}$), $\dot{V}_{Ei}$ is the mean $\dot{V}_{Ei}$ for each activity i ($L \cdot min^{-1}$), t_i is the time spent at each activity i ($min \cdot day^{-1}$), i is activity during the day, k is the number of activities, and 10^{-3} is a conversion factor. The critical issue in this approach is the need to accumulate adequate data for $\dot{V}_E$ during short-term activities throughout the day. However, there have been quite limited experimental data on $\dot{V}_E$ for children, especially for moderate-to-vigorous levels of physical activity and the habitual activities of daily life. The absence of data for children has been a source of error in estimations of daily inhalation rate by the time-activity-ventilation method. For example, Brochu[12] reported that the time-activity-ventilation approach can lead to an overestimation of the daily inhalation rates in 5- to 12-yr-old children by 75% because of the lack of $\dot{V}_E$ data for children during different levels of activities in daily life.

Another limitation of the time-activity-ventilation method is the availability of suitable techniques to obtain the intensity and duration of physical activity of young children during daily life. Self-report activity diaries and heart rate monitoring are the traditional tools used to determine the level of physical activity for estimating the $\dot{V}_E$ of free-living people. The disadvantages of self-reporting are that it tends to be subjective and is not practical for the assessment of young children, who are unable to accurately self-estimate and record their physical activity levels.[13–15] Even if an observer records the activities of children, it is still not possible to accurately measure the intensity and duration of the activities of children, which can vary within a few seconds.[16,17] Heart rate is a valid predictor of $\dot{V}_E$,[18] but its limitations include interruption of heart rate measurement by electrode displacement and discomfort from the electrodes, which can reduce the

compliance of children and their parents with the study requirements.[15] To overcome these issues in monitoring the activity of children, an accelerometer could be a practical alternative for measuring the intensity, frequency, and duration of physical activity of free-living people. The advantages of an accelerometer-based approach are that it is noninvasive, it is not affected by the wearing of clothes, and it can provide data on a second time scale over long periods of time without interfering with normal activities. Many studies have examined the reliability and validity of these devices in children under laboratory and field conditions and determined that they provide valid measures of EE and oxygen (O_2) consumption in children.[19–31]

The primary goal of this study was to develop a regression equation to predict $\dot{V}_E$ from accelerometer measurements to estimate the daily inhalation rate in young children. First evaluated was the validity of accelerometer measurements to predict $\dot{V}_E$ by calibrating the Actical omniaxial accelerometer and the ActivTracer triaxial accelerometer against the $\dot{V}_E$ measured at different levels of activity by the Douglas bag method. The performance of the accelerometers was also evaluated by comparing the accelerometer measurements with heart rate.

METHODS
Participants and Study Design

The study presented here was conducted from December 2006 through March 2007. The study population comprised 29 Japanese preschool children (16 boys and 13 girls) 6 yr of age (mean age, 6.5 ± 0.2 years) who were recruited from a single kindergarten class thanks to the cooperation of the administrative personnel. The children's mean height was 115.4 cm (SD, 5 cm; range, 103.4–124.6 cm) and mean body weight was 20.6 kg (SD, 2.4 kg; range, 17–26.3 kg); these data were obtained at the start of the experiment. The V_E associated with nine different levels of physical activity were measured in a laboratory setting. Body acceleration and heart rate were measured by using activity and heart rate monitors and these measures were calibrated against the $\dot{V}_E$ values. Written informed consent was obtained from the parents of each participant. The ethics committee of the National Institute (Tsukuba, Ibaraki, Japan) approved the experimental protocol for Environmental Studies.

Procedure

The experiment was conducted in a recreation room of the kindergarten from 2:00 to 6:00 p.m. Room temperature was set between 23 and 25 °C throughout the experiment to avoid the influence of cold temperature on the metabolism of the participants.[32,33] All participants had fasted for at least 2 hr before the experiment to avoid an increase in metabolic rate.[33] At the start of the experiment, participants first lay on a floor mat without movement for at least 30 min to allow their metabolic rate to stabilize. After this equilibrating period, expired breath was collected for the resting state over 10 min. The participants then sequentially performed eight activities: (1) sitting in a chair, (2) standing, (3) playing with plastic bricks, (4) building with blocks, (5) walking, (6) climbing stairs (up and down), (7) tossing a ball, and (8) running. When the participants were sitting or standing, they were

asked to keep calm and watch a cartoon video for 10 min. The children played for 15 min with the plastic bricks while sitting in a chair at a desk. When building with blocks, participants were allowed to move freely within a 1.9- by 2.4-m area of free space for 5 min; this activity included standing, squatting, walking, and lifting and carrying blocks. For climbing stairs, participants repeated climbing up and down four steps for 2 min. For ball tossing, a handball was thrown to the participant from a set distance every 7 sec for 3 min; participants were asked to catch the ball and throw it back. For walking, participants were instructed to walk continuously at their normal pace along a straight course of 10 m for 4 min. Running was performed for 3 min under the same conditions as walking, but participants were encouraged to maintain a speed of more than $100 \text{ m} \cdot \text{min}^{-1}$.[34] The average speed was $69 \pm 6.4 \text{ m} \cdot \text{min}^{-1}$ for walking and $133 \pm 17 \text{ m} \cdot \text{min}^{-1}$ for running. The activities were chosen because they are commonly performed by children and cover a wide range of activity levels on the basis of observations in the kindergarten and because they were thought not to interrupt the breath sampling described below.

The $\dot{V}_E$ during the nine different activities was measured by the Douglas bag method. During each activity, participants wore facemasks to collect expired breath. Expired breath was collected through tubes (2.5-cm inner diameter × 80-cm length) into the 50-L Douglas bag near the end of each activity, after O_2 consumption ($\dot{V}O_2$) had stabilized. Previous studies have reported that $\dot{V}O_2$ and heart rate almost reach a plateau 1–2 min after the start of a 5-min endurance run in children 5 yr of age.[35,36] The durations of the activities and sampling periods are summarized in Table 1.

Instruments

Body acceleration was recorded throughout the experiment by using an Actical accelerometer (27 × 28 × 10 mm, 17 g, Mini-mitter, Inc.) and an ActivTracer accelerometer (type AC-210A, 48 × 67 × 16 mm, 57 g, GMS, Inc.). These two acceleration monitors were selected because of superior technical support and the following reasons. The Actical was selected because it was small, lightweight, and was considered to be suitable for invasive monitoring of activities of young children. The ActivTracer was selected because triaxial accelerometers

have been reported to capture the principal acceleration component, which varies considerably with type of activity (e.g., between arm work and walking)[21,22] and would thus more accurately measure the free-living activities of children than uniaxial accelerometers. This notion is supported by a previous report that the output from a triaxial accelerometer provides a stronger correlation with $\dot{V}O_2$ than that of a uniaxial accelerometer.[23]

The Actical accelerometer has an omnidirectional sensor that is sensitive to movements in all directions and is most sensitive to vertical movement when mounted on the hip. The sensor detects movements in the 0.5- to 3.2-Hz frequency range and generates an analog voltage. The voltage is amplified, filtered, and then digitized by an analog-to-digital converter to create a digital value. The process is repeated 32 times per second (32 Hz), or every 31.25 msec, and the 32 digitized values in 1 sec are summed. The resulting 1-sec value is divided by 4 and then added to an accumulated activity value for the time intervals (epoch) specified by the user. The Actical accelerometer provides the measurements in terms of activity counts.

The ActivTracer accelerometer contains a triaxial accelerometer that detects movements in the anteroposterior (x-axis), mediolateral (y-axis), and vertical (z-axis) directions. The sensor detects the movements in each of the three directions every 40 msec with a band-pass filter of 0.3–100 Hz. The measurement range of the sensor is 0 to ±4 G for the vertical direction and 0 to ±2 G for the anteroposterior and mediolateral directions, and the resolution is 0.002 G. The output measure of the ActivTracer is the average of absolute values for acceleration (mG) in each axis direction and a synthesis of acceleration in three directions (xyz, vector synthetic) for the time interval defined by the user. Note that the outputs of the two accelerometers are not comparable because each provides acceleration measurement through a different data processing algorithm.

During the experiment, participants wore the two accelerometers on the hip by using a belt (Figure 1). Heart rate was also monitored (ActiHR, Mini-mitter, Inc.) to compare the validity of the measurement for predicting $\dot{V}_E$ with the accelerometer measurement. The sensor and lead of the heart rate monitor were attached to the participant's chest using disposable electrode pads in accordance with the manufacturer's instructions. Acceleration and heart rate were monitored every 15 sec.

The volume of expired breath was measured with a dry gas flow meter (Shinagawa Company). To measure $\dot{V}O_2$ and carbon dioxide (CO_2) production by participants, the O_2 and CO_2 concentrations in expired breath were analyzed by using a portable gas analyzer (AR-1, ARCO System, Inc.), which was calibrated and verified with outdoor air before each sample analysis.

Data Analysis
The volume of expired breath measured at ambient temperature and pressure and saturated with water vapor (ATPS condition) was converted to the volume at standard temperature and pressure under dry conditions (STPD condition). With the exception of the data for running, if the respiratory quotient (which is expressed as the ratio between

Table 1. Time periods for performance of physical activity and sampling of exhaled breath.

Activity	Time for Performance (min)	Time for Breath Sampling (min)
Lying	30	10
Sitting	10	5
Standing	7	5
Playing plastic bricks	10	5
Building with blocks	5	2
Walking	4	2
Climbing stairs	3	1
Ball tossing	3	1
Running	3	1

Figure 1. Children wearing Actical and ActivTracer accelerometers on their hips with a belt. Heart rate was monitored at the same time using an ActiHR attached to the participant's chest. Dashed lines indicate the location of the sensor and lead of the heart rate monitor under the clothing.

CO_2 production [$\dot{V}CO_2$] and $\dot{V}O_2$) was outside of the range 0.75–0.99, the V_E data were excluded from the analysis because the participant was in a state of hyperventilation or the exhaled breath had leaked from the facemask during breath sampling. Mean height, body weight, and V_E values were compared between boys and girls by using the Student's t test. For comparison of acceleration among multiple activities, one-way analysis of variance (ANOVA) was conducted, followed by the Scheffe test for the individual comparison if the result of ANOVA was significant.

Linear regression analysis was performed to develop equations to predict $\dot{V}_E$ from the synthetic acceleration from the accelerometers and heart rates with all of the participants and activities combined. The regression equations were presented as follows:

$$y = a + b \times x \qquad (2)$$

where y is $\dot{V}_E$ as an independent variable and x is the synthetic acceleration or heart rate as a dependent variable. The $\dot{V}_E$ for each activity and participant was estimated from the linear regression equation. To evaluate the validity, the $\dot{V}_E$ estimated from activity counts measured by the Actical and ActivTracer and from heart rate measurements were individually compared with the $\dot{V}_E$ measured by the Douglas bag method. The percentage differences were then calculated for each activity using a technique developed by Bland and Altman to assess the agreement between two methods of measurement.[37]

Using the vertical and horizontal acceleration measured by the ActivTracer, linear discriminant analysis was performed to identify variables that strongly discriminate between the different types of activities. This analysis was used to dichotomize the type of activity into two groups, group 0 and group 1, and group was included in the analysis as a categorical dependent variable. The vertical activity counts (z) and the ratio between vertical and horizontal acceleration ($z/[x^2 + y^2]^{0.5}$) were included as independent variables. The significance of the discriminant function was evaluated with Wilks' λ. All statistical analyses were performed using SPSS software version 15 for Windows (SPSS, Inc.). Statistical significance was set at $P < 0.05$.

The physical activity ratio (PAR), which is the energy cost of an activity per unit time, was calculated to classify V_E according to the intensity of physical activity on the basis of energy consumption. The PAR was calculated by dividing the EE (kcal $\cdot$ min^{-1}) for a specific activity by the estimated basal metabolic rate (BMR).[38,39] EE was calculated from the $\dot{V}O_2$ (L $\cdot$ min^{-1}) and $\dot{V}CO_2$ (L $\cdot$ min^{-1}) as described previously.[40] BMR was calculated by dividing the EE during the resting state by 1.1 on the assumption that the thermic effect of food is 10% of the BMR.[32] PAR was categorized as sedentary (PAR < 1.5), light ($1.5 \leq$ PAR < 3), moderate ($3 \leq$ PAR < 6), and vigorous ($6 \leq$ PAR) according to values given in the literature for the energy cost of physical activities.[26] All data in the text, tables, and figures are presented as mean $\pm$ 1 SD.

RESULTS

The $\dot{V}_E$ (STPD), $\dot{V}O_2$ (STPD), accelerometer measurements, and heart rates of participants during the nine physical activities are summarized in Tables 2 and 3. The $\dot{V}_E$ ranged from 0.18 $\pm$ 0.02 L $\cdot$ kg^{-1} $\cdot$ min^{-1} when the participant was lying down to 1.07 $\pm$ 0.29 L $\cdot$ kg^{-1} $\cdot$ min^{-1} during running. There were no gender-associated differences ($P > 0.05$, t test) in the height or weight of participants or in $\dot{V}_E$ during the various activities.

Table 2. Summary of V_E and $\dot{V}O_2$ at STPD and PAR during nine different activities.

Activity	n	$\dot{V}_E$ (STPD) L $\cdot$ min^{-1}	$\dot{V}_E$ (STPD) L $\cdot$ kg^{-1} $\cdot$ min^{-1}	$\dot{V}O_2$ (STPD) L $\cdot$ kg^{-1} $\cdot$ min^{-1}	PAR
Lying	27	3.9 ± 0.5	0.18 ± 0.02	0.006 ± 0.001	–
Sitting	24	4.4 ± 0.6	0.21 ± 0.02	0.007 ± 0.001	1.15 ± 0.77
Standing	25	4.5 ± 0.6	0.22 ± 0.03	0.007 ± 0.001	1.19 ± 0.21
Playing plastic bricks	28	5.1 ± 0.7	0.25 ± 0.03	0.008 ± 0.001	1.37 ± 0.36
Building with blocks	28	10.5 ± 1.7	0.51 ± 0.09	0.017 ± 0.003	2.98 ± 0.68
Walking	24	9.7 ± 1.5	0.47 ± 0.06	0.016 ± 0.002	2.80 ± 0.48
Climbing stairs	28	16.5 ± 3.3	0.81 ± 0.12	0.028 ± 0.004	4.79 ± 0.83
Ball tossing	28	15.4 ± 3.1	0.75 ± 0.12	0.026 ± 0.004	4.55 ± 0.89
Running	28	22.8 ± 4.8	1.07 ± 0.29	0.032 ± 0.005	5.74 ± 0.23

Table 3. Summary of accelerometer measurements and heart rate during nine different activities.

Activity	Actical (counts · 15 sec⁻¹)		ActivTracer (mG · 15 sec⁻¹)				Heart Rate (beats · min⁻¹)	
	n	Synthetic	n	Synthetic	Vertical	Horizontal	n	
Lying	27	2 ± 4	27	7 ± 5	2 ± 2	6 ± 4	27	98 ± 9
Sitting	27	1 ± 3	28	15 ± 7	3 ± 2	11 ± 6	28	101 ± 10
Standing	29	5 ± 9	29	19 ± 11	6 ± 5	15 ± 8	29	102 ± 22
Playing with plastic bricks	27	23 ± 38	27	38 ± 16	7 ± 4	31 ± 13	25	111 ± 9
Building with blocks	26	217 ± 133	26	205 ± 57	116 ± 49	128 ± 26	26	134 ± 16
Walking	24	523 ± 176	24	341 ± 70	241 ± 62	179 ± 31	25	131 ± 13
Climbing stairs	24	772 ± 160	24	441 ± 78	321 ± 69	217 ± 34	24	162 ± 12
Ball tossing	26	673 ± 210	26	426 ± 94	293 ± 91	223 ± 29	26	161 ± 16
Running	26	1960 ± 370	25	1024 ± 126	855 ± 118	386 ± 70	27	177 ± 14

Synthetic acceleration ranged from 1 ± 3 counts · sec⁻¹ during sitting to 1960 ± 370 counts · sec⁻¹ during running when measured with the Actical accelerometer and from 7.4 ± 5.2 during lying down to 1024 ± 126 mG · sec⁻¹ during running with the ActivTracer accelerometer. The ActivTracer detected body acceleration in all participants during all nine activities. By comparison, the Actical detected body acceleration in only 78% of participants when lying down, 61% during sitting, 90% during standing, 75% while playing with plastic blocks, and in 100% of participants during all other activities. A significant difference was observed among the accelerations for resting, sitting, standing, and building with blocks when measured with the ActivTracer, whereas no significant difference was observed among the accelerations for these four activities when measured with Actical (ANOVA, $P <$ 0.05). Heart rates ranged from 98 ± 9 beats · min⁻¹ when the participant was lying down to 177 ± 14 beats · min⁻¹ during running.

Calibration

There was a strong correlation between the experimentally measured $\dot{V}_E$ using the Douglas bag method and the synthetic acceleration measured by the Actical and ActivTracer; Pearson's correlation coefficients were r =

0.886 ($n = 223$, $P < 0.001$) for the Actical and 0.913 ($n = 222$, $P < 0.001$) for the ActivTracer. Heart rates showed a high linear correlation with the logarithmic $\dot{V}_E$ (r = 0.909, $n = 223$, $P < 0.001$).

The mean percentage differences between experimentally measured $\dot{V}_E$ and that estimated from synthetic acceleration and heart rates were calculated using linear regression models (Table 4). The synthetic acceleration overestimated $\dot{V}_E$ from lying down through playing with plastic bricks by 24–60% for the Actical and by 14–37% by the ActivTracer. $\dot{V}_E$ values for walking and running were overestimated by 11–20% for the Actical and by 11–24% for the ActivTracer. By comparison, the Actical underestimated the $\dot{V}_E$ values for building with blocks, ball tossing, and stair climbing by 19–23%, and the ActivTracer underestimated these values by 13–18%. When predicted from heart rates, $\dot{V}_E$ for lying down through to playing with plastic bricks was overestimated by 14–19%, whereas that for walking through to running was underestimated by 2–11%, with the exception of ball tossing, which was within an overestimation of 1%. The overall mean differences between the observed and predicted $\dot{V}_E$ were greater for the Actical (13% ± 33%) and ActivTracer (9% ± 24%) than for those calculated from heart rates (4% ± 26%).

Table 4. Difference between observed and estimated $\dot{V}_E$ from Actical and ActivTracer accelerometer measurements and heart rate using a single regression equation.

Activity	Actical		ActivTracer[a]		Heart Rate	
	Difference (L · kg⁻¹ · min⁻¹)	Percent Difference	Difference (L · kg⁻¹ · min⁻¹)	Percent Difference	Difference (L · kg⁻¹ · min⁻¹)	Percent Difference
Lying	0.11 ± 0.02	60.0 ± 22.5	0.06 ± 0.02	36.6 ± 19.0	0.03 ± 0.04	18.7 ± 23.5
Sitting	0.09 ± 0.02	43.0 ± 17.6	0.05 ± 0.02	24.6 ± 15.3	0.03 ± 0.05	13.8 ± 25.1
Standing	0.08 ± 0.03	37.3 ± 19.8	0.04 ± 0.03	21.8 ± 17.6	0.04 ± 0.06	19.7 ± 32.6
Playing plastic bricks	0.05 ± 0.03	24.1 ± 17.1	0.03 ± 0.03	14.1 ± 14.1	0.03 ± 0.04	13.9 ± 17.4
Building with blocks	−0.13 ± 0.04	−22.7 ± 13.9	−0.09 ± 0.07	−15.0 ± 12.1	−0.06 ± 0.10	−11.4 ± 19.4
Walking	0.06 ± 0.07	14.1 ± 14.4	0.09 ± 0.07	20.4 ± 15.1	−0.05 ± 0.10	−10.2 ± 20.3
Climbing stairs	−0.16 ± 0.11	−18.7 ± 11.0	−0.15 ± 0.11	−17.5 ± 12.3	−0.02 ± 0.16	−2.2 ± 20.9
Ball tossing	−0.15 ± 0.11	−18.7 ± 12.4	−0.11 ± 0.12	−13.5 ± 13.9	0.01 ± 0.19	0.6 ± 24.3
Running	0.08 ± 0.25	10.7 ± 24.9	0.08 ± 0.21	10.9 ± 20.9	−0.04 ± 0.27	−3.1 ± 23.9

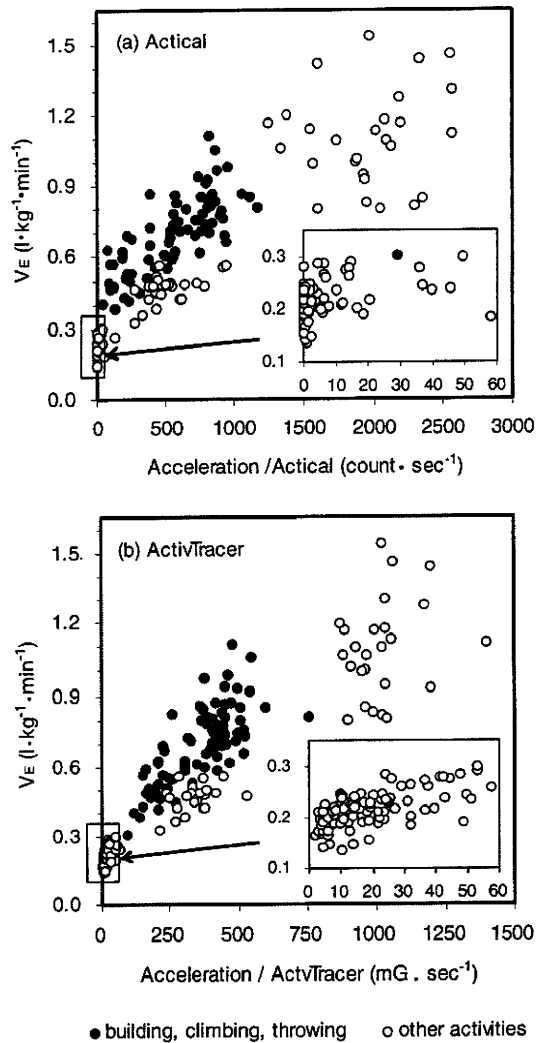*Notes:* [a]Results of estimation using a single regression equation are presented.

$$f = -3.31 + 5.98 \times (z/[x^2 + y^2]^{0.5}) - 0.017 \times z$$

$$(3)$$

The standardized canonical coefficient was greater for the ratio between vertical and horizontal acceleration than for vertical acceleration alone, indicating that the ratio was a more significant discriminator than the vertical acceleration. The sensitivity of discrimination was 75% for group 1 (walking) and 70% for group 0 (other activities). The correct classification rate was 75% for walking, as category 1, and was 60, 64, and 89% for the category 0 activities building with blocks, stair climbing, and ball tossing, respectively.

The $\dot{V}_E$ for each activity was recalculated in two steps for data obtained with the ActivTracer. When the synthetic acceleration of a given activity was between 96 and 754 mG · sec^{-1} (the range of accelerometer measurements by the ActivTracer from building with blocks through to ball tossing), the activity was classified as walking or other activities using the previously described discriminant function. The $\dot{V}_E$ then was estimated from the synthetic acceleration measured by the ActivTracer using the regression equation developed for the group of activities to which the activity of interest was classified. As a result, the mean difference between observed and estimated $\dot{V}_E$ was +10% for lying down, +1% for sitting, −1% for standing, −6% for playing with plastic bricks and building with blocks, +16% for walking, −12% for stair climbing, −0.3% for ball tossing, and +1% for running (Figure 3). The overall mean percentage difference was 0.2% ± 19% (−0.01 ± 0.12 L · kg^{-1} · min^{-1}).

Classification of $\dot{V}_E$

The mean PAR was 1.16 ± 0.07 for sitting, 1.20 ± 0.11 for standing, 1.38 ± 0.20 for playing with plastic bricks, 2.79 ± 0.48 for walking, 3.00 ± 0.56 for building with
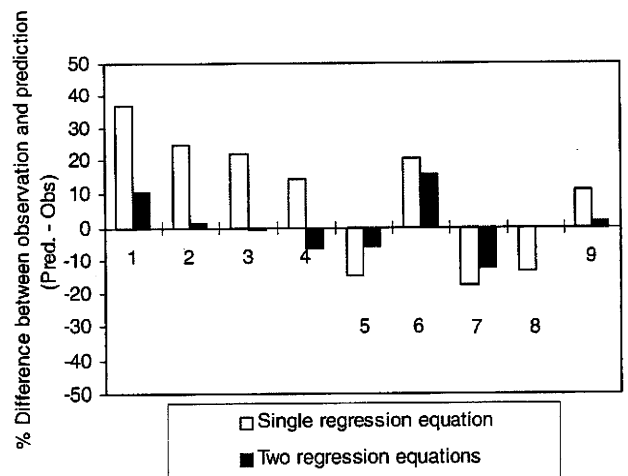
Figure 2. Scatterplots of $\dot{V}_E$ vs. accelerometer measurement (vector synthesis): (a) Actical and (b) ActivTracer. Activities were divided into two groups: (1) building, climbing, and throwing and (2) all other activities.

Additional regression analysis showed that when building with blocks, ball tossing, and stair climbing were excluded, the correlation between $\dot{V}_E$ and synthetic acceleration was improved, with r = 0.949 (n = 146, P < 0.001, y = 0.0004x + 0.22) for the Actical and r = 0.962 (n = 145, P < 0.001, y = 0.00086x + 0.20) for the ActivTracer. For the group of activities including building with blocks, ball tossing, and stair climbing, the correlation between V_E and synthetic acceleration was r = 0.781 (n = 77, P < 0.001, y = 0.0004x + 0.44) for the Actical and r = 0.761 (n = 77, P < 0.001, y = 0.00094x + 0.35) for the ActivTracer (Figure 2).

Activity Type by Using Vertical and Horizontal Activity Counts

The linear discriminant analysis showed a significant difference between walking and the group of activities comprising building with blocks, stair climbing, and ball tossing (Wilks' λ = 0.897, P < 0.005). The discriminant function obtained was

Figure 3. Percent difference between $\dot{V}_E$ measured with a Douglas bag and that predicted from synthetic accelerometer measurements by the ActivTracer during nine different activities. Percent differences using the two regression equations were compared with those using the single regression equation. Activity: 1 = lying down, 2 = sitting, 3 = standing, 4 = playing with plastic bricks, 5 = building with blocks, 6 = walking, 7 = stair climbing, 8 = ball tossing, and 9 = running.

blocks, 4.84 ± 0.68 for climbing stairs, 4.54 ± 0.91 for ball tossing, and 5.79 ± 1.05 for running. The PAR indicates a sedentary state for sitting, standing, and playing with plastic bricks; a light-to-moderate level of physical activity for building with blocks and walking; moderate physical activity for stair climbing and ball tossing; and moderate-to-vigorous physical activity for running. The thresholds corresponding to PAR values of 1.5, 3, and 6, which are the cutpoints between sedentary-to-light, light-to-moderate, and moderate-to-vigorous levels of physical activity intensity were 132, 478, and 1783 counts · sec^{-1} for the Actical measurements and 71, 412, and 1093 mG · sec^{-1} (category 1) and 31, 218, and 593 mG · sec^{-1} (category 0) for the ActivTracer measurements.

DISCUSSION

In the study presented here, mean $\dot{V}_E$ values were obtained for Japanese preschool children 6 yr of age during the resting state and during sedentary through to vigorous physical activity. The weight and height of the participants in this study were similar to those reported for 6-yr-old children by the Ministry of Health, Labor, and Welfare, Japan.[41] The $\dot{V}_E$ values presented here for sitting and standing, which were equivalent to 5.00 ± 0.64 and 5.23 ± 0.67 L · min^{-1}, respectively, at body temperature, ambient pressure, and saturated with water vapor (BTPS) were consistent with the $\dot{V}_E$ values of 4.98 ± 0.56 and 5.48 ± 0.44 L · min^{-1} (BTPS) in children 4–6 yr of age reported by Honda.[42]

The accelerometer measurements were also validated for estimating the $\dot{V}_E$ of young children during daily life. To the authors' knowledge, this study is the first to use accelerometer-based activity measurements to estimate $\dot{V}_E$ for different levels of activity. There was a strong positive linear correlation between synthetic acceleration from the accelerometers and $\dot{V}_E$ from the resting state through to vigorous physical activity, indicating that accelerometers can be used to estimate $\dot{V}_E$.

The comparison between the Actical and ActivTracer accelerometers presented here revealed smaller percentage differences between observed and predicted values with the ActivTracer, especially from resting through to light levels of physical activity. This result suggests that the ActivTracer more accurately measures physical activity and hence $\dot{V}_E$ than does the Actical. This difference is largely because of the differences in the ability of the Actical and ActivTracer to sense body acceleration. The ActivTracer detected body acceleration during resting and sedentary activities in all participants and revealed significant differences among the accelerations for resting, sitting, standing, and building with blocks. In contrast, the Actical failed to detect body movement in all participants during these activities and could not detect differences in acceleration among the activities. On the basis of the correlation coefficients for the single linear regression model, heart rate was a better predictor of $\dot{V}_E$ than the synthetic acceleration measurements from the accelerometers, but there was poor agreement between observed and predicted $\dot{V}_E$ from the resting state through to light levels of activity.

The primary limitation of accelerometers for estimating $\dot{V}_E$ is that a single regression model does not accurately predict the $\dot{V}_E$ associated with activities during daily life. This study showed that the $\dot{V}_E$ for building with blocks, stair climbing, and ball tossing was underestimated by using the synthetic acceleration from the Actical and ActivTracer accelerometers. The experimentally observed $\dot{V}_E$ was significantly higher for these three activities than for walking, although activity counts for all of these activities varied similarly. This variability in the relationship between $\dot{V}_E$ and synthetic acceleration resulted in marked differences between observed data and estimated values derived using the single regression model. Similar results have been reported in studies validating the use of accelerometer-based activity monitors for determining EE.[43,44] The underlying explanation is that static work or upper body activities such as lifting, carrying, and throwing objects results in increased EE or $\dot{V}O_2$,[45–49] and thus an increase in $\dot{V}_E$, without a proportional increase in body movement. This discrepancy cannot be captured by synthetic acceleration alone.

It was shown that the type of activity can be discriminated by using three-dimensional motion data obtained from a triaxial accelerometer. Discriminant analysis revealed that the ratio between vertical and horizontal acceleration and vertical acceleration alone were reasonably effective in discriminating walking from playing with plastic bricks, climbing stairs, and ball tossing as a group but were less effective in discriminating between playing with plastic bricks and climbing stairs. The study presented here also demonstrated that prediction of $\dot{V}_E$ can be improved through discrimination of the type of activity using the three-dimensional motion data and use of one of two regression models specific for the type of activity. Using this approach, the percentage difference between observed and predicted $\dot{V}_E$ was improved for each activity by an average of 14% and was even smaller than those predicted from heart rate (Table 4 and Figure 3).

This approach for improving the accuracy of estimating $\dot{V}_E$ is essential for the more accurate assessment of the short-term or daily dose of air pollutants through inhalation, especially from the resting state through to light physical activity, because people tend to spend the greatest proportion of time at these levels of activity.[50,51] For example, for lying down, the 37% overestimation in $\dot{V}_E$ resulting from the single regression equation with all activities combined is estimated to result in an overestimation of 8.6% in daily inhalation volume given the assumption that in 1 day children spend 10.2 hr in a resting state; 4 hr in a sedentary state; and 8.3, 1.3, and 1.2 hr in light, moderate, and vigorous levels of physical activity, respectively.[52] By comparison, the 10% overestimation in $\dot{V}_E$ for lying down calculated by the two regression equations is estimated to result in only a 2% overestimation in daily inhalation volume using the same assumptions.

Misclassification of the activity type by the discriminant function still leads to inaccurate estimations of $\dot{V}_E$ for walking and climbing stairs. Using the assumption described above, a 16% error in the estimation for light-level activities (e.g., walking) is roughly equivalent to 7%

of the total daily inhalation volume. However, an overestimation of $\dot{V}_E$ can be canceled out, at least in part, by underestimation of V_E for other light-to-moderate activities (e.g., building with blocks and stair climbing). Underestimation of $\dot{V}_E$ for climbing stairs will not cause considerable error because generally people spend only brief amounts of time in this type of activity during daily life.

The study presented here demonstrates that accelerometer measurements are a valid predictor of $\dot{V}_E$ in children and overcome some of the limitations of traditional approaches. The traditional approach using self-report activity diaries has limited objectivity and accuracy in quantifying the intensity of physical activity of free-living people. For example, Bender[16] conducted a study of 65 children aged 10–16 yr together with their parents and reported a poor correlation between proxy records of children's physical activity by parents and the metabolic equivalent value on the basis of accelerometer measurements as an objective measure of physical activity ($r \leq$ 0.383). In another study, Lichtman[53] reported that the actual daily EE, measured by the DLW method, was overestimated by 50% in self-report activity diaries for adults. The inherent inability of self-reports to accurately quantify the intensity of physical activity could thus result in errors in estimating the daily inhalation rate. The validity of accelerometers in estimating $\dot{V}_E$ was estimated by comparing measurements from them with measurements from the Douglas bag method, and it was found that the correlation between accelerometer measurement and $\dot{V}_E$ is strong and that the error in estimating $\dot{V}_E$ using the regression equations derived from ActivTracer measurements is between -12% and $+16\%$ depending on the activity. Also, this difference was smaller than those estimated from the heart rate measurements.

Standards for categorizing $\dot{V}_E$ have not been defined for children. Here, $\dot{V}_E$ was classified in relation to the level of physical activity for children in terms of the PAR. Differences in this classification structure between studies might lead to differences in the $\dot{V}_E$ corresponding to the activity level of interest and the estimates of the time spent in activities of different intensity categories. A previous study[54] presented V_E corresponding to the level of physical activity intensity described in terms of metabolic equivalents (METs), which are expressed as a multiple of the resting metabolic rate for an activity. One MET is generally considered equivalent to the resting $\dot{V}O_2$ of 3.5 mL $\cdot$ kg^{-1} $\cdot$ min^{-1} in adults. However, in children, the resting metabolic rate is known to exceed 3.5 mL $\cdot$ kg^{-1} $\cdot$ min^{-1}.[26,55] Puyau et al.[24] reported that use of the adult default value resulted in significant differences between the observed PAR and estimated MET and that this difference was greater in younger children and at higher levels of EE. Thus, use of the adult default value would inaccurately reflect the level of intensity of physical activities in young children.

One of the shortcomings of this study is the small number of subjects. Further studies with a larger study group would more accurately represent the population of 6-yr-old children in Japan. Repeated measurements of $\dot{V}_E$ are also needed to obtain a more reliable assessment of $\dot{V}_E$ in young children. The conclusions presented here are based on nine different levels of physical activity in a laboratory setting and provide strong groundwork for further analysis and research. Additional studies covering a more comprehensive range of activities are needed to confirm the validity of this approach for prediction of $\dot{V}_E$ and to better understand the factors that contribute to variability in accelerometer measurements.

REFERENCES
1. Strategic Approach to International Chemical Management (SAICM), Report of the International Conference on Chemicals Management on the Works of Its First Session; available at http://www.chem.unep.ch/ICCM/meeting_docs/iccm1_7/7%20Report%20E.pdf (accessed April 19, 2010).
2. A Framework for Assessing Health of Environmental Exposures to Children; EPA/600/R-05/093F; U.S. Environmental Protection Agency; National Center for Environmental Assessment: Washington, DC, 2006; available at http://www.epa.gov/ncea (accessed April 19, 2010).
3. Principle for Evaluating Health Risks in Children Associated with Exposure to Chemicals; Environmental Health Criteria 237; World Health Organization: Geneva, Switzerland 2006.
4. Report on Committee for Setting Goal for Reducing the Level of Dioxin in the Atmosphere; Japan Environment Agency: Tokyo, Japan, 1997.
5. Brochu, P.; Robitaille, D.; Francois, J.; Brodeur, J. Physiological Daily Inhalation Rates for Free Living Individuals Aged 1 Month to 96 Years Using Data from Doubly Labeled Water Measurements: A Proposal for Air Quality Criteria, Standard Calculations and Health Risk Assessment; Hum. Ecol. Risk Assess. 2007, 12, 675-701.
6. Spiers, C.E.; Little, D.E.; Trim, S.C.; Johnson, T.R. Linn; W.S.; Hackney, J.D. Activity Patterns in Elementary and High School Students Exposed to Oxidant Pollution; J. Expo. Anal. Environ. Epidemiol. 1992, 2, 277-293.
7. Allan, M.; Richardson, G.M. Probability Density Functions Describing 24-Hour Inhalation Rates for Use in Human Health Risk Assessment; Hum. Ecol. Risk Assess. 1998, 4, 379-408.
8. Layton, D.W. Metabolically Consistent Breathing Rates for Use in Dose Assessment; Health Phys. 1993, 64, 23-36.
9. McCurdy, T. Conceptual Basis for Multi-Route Intake Dose Modeling Using an Energy Expenditure Approach; J. Expo. Anal. Environ. Epidemiol. 2000, 10, 86-97.
10. Exposure Factors Handbook; U.S. Environmental Protection Agency; National Center for Environmental Assessment; Office of Research and Development: Washington, DC, 1997.
11. Child-Specific Exposure Factors Handbook; EPA/600/R-06/096F; U.S. Environmental Protection Agency; National Center for Environmental Assessment; Office of Research and Development: Washington, DC, 2008.
12. Brochu, P.; Robitaille, D.; Francois, J.; Brodeur, J. Physiological Daily. Inhalation Rates for Free Living Individuals Aged 2.6 Month to 96 Years Based on Doubly Labeled Water Measurements: Comparison with Time-Activity-Ventilation and Metabolic Energy Conversion Estimates; Hum. Ecol. Risk Assess. 2006, 12, 736-761.
13. Sallis, J.F. Self Report Measures of Children's Physical Activity; J. Sch. Health. 1991, 61, 215-219.
14. Coleman, K.J.; Saelens, B.E.; Wiedrich-Smith, M.D.; Finn, J.D.; Epstein, L.H. Relationships between TriTrac-R3D Vectors; Heart Rate, and Self Report in Obese Children; Med. Sci. Sports Exerc. 1997, 29, 1535-1542.
15. Terblanche, A.P.S.; Ozkaynak, H.; Spengler, J.D.; Butler, D.A. Relationship between Self Reported Activity Levels and Actual Heart Rates in Teenagers; J. Air & Waste Manage. Assoc. 1991, 41, 942-946.

16. Bender, J.M.; Brownson, R.C.; Elliott, M.B., Haire-Joshu, D.L. Children's Physical Activity: Using Accelerometers to Validate a Parent Proxy Record; *Med. Sci. Sports Exerc.* **2005**, *37*, 1409-1413.
17. Bailey, R.C.; Olson, J.; Pepper, S.L.; Porszasz, J.; Barstow, T.J.; Cooper, D.M. The Level and Tempo of Children's Physical Activities: An Observational Study; *Med. Sci. Sports Exerc.* **1995**, *27*, 1033-1041.
18. Adams, W.C. *Measurement of Breathing Rate and Volume in Routinely Performed Daily Activities*; Contract No. A033-205, Final Report; California Environmental Protection Agency; Air Resources Board: Sacramento, CA, 1993.
19. Welk, G.J. Measurement Issues in the Assessment of Physical Activity in Children; *Res. Q. Exerc. Sport.* **2000**, *71*, 59-73.
20. Meijer, G.A.; Westerterp, K.R.; Koper, H.; Hoor, F.T. Assessment of Energy Expenditure by Recording Heart Rate and Body Acceleration; *Med. Sci. Sports Exerc.* **1989**, *21*, 343-347.
21. Bouten, C.V.; Westerterp, K.R.; Verduin, V.; Janssen, J.D. Assessment of Energy Expenditure for Physical Activity Using a Triaxial Accelerometer; *Med. Sci. Sports Exerc.* **1994**, *26*, 1516-1523.
22. Eston, R.G.; Rowlands, A.V.; Ingledew, D.K. Validity of Heart Rate; Pedometry and Accelerometry for Predicting Energy Cost of Children's Activities; *J. Appl. Physiol.* **1998**, *84*, 362-371.
23. Ott, A.E.; Pate, R.R.; Trost, S.G.; Ward, D.S.; Saunders, R. The Use of Uniaxial and Triaxial Accelerometers to Measure Children's "Free Play" Activity; *Pediatr. Exerc. Sci.* **2000**, *12*, 360-370.
24. Puyau, M.R.; Adolph, A.L.; Vohra, F.A.; Butte, N.F. Validation and Calibration of Physical Activity Monitors in Children; *Obes. Res.* **2002**, *10*, 150-157.
25. Rodriguez, G.; Beghin, L.; Michaud, L.; Moreno, L.A.; Turck, D.; Gottrand, F. Comparison of the TriTrac-R3D Accelerometer and a Self-Report Activity Diary with Heart-Rate Monitoring for the Assessment of Energy Expenditure in Children; *Br. J. Nutr.* **2002**, *87*, 623-631.
26. Puyau, M.R.; Adolph, A.L.; Vohra, F.A.; Zakeri, I.; Butte, N.F. Prediction of Activity Energy Expenditure Using Accelerometers in Children; *Med. Sci. Sports Exerc.* **2004**, *36*, 1625-1631.
27. Pfeiffer, K.A.; McIver, K.L.; Dowda, M.; Almeida, M.J.; Pate, R.R. Validation and Calibration of the Actical Accelerometer in Preschool Children; *Med. Sci. Sports Exerc.* **2006**, *38*, 152-157.
28. Trost, G.; Ward, D.S.; Moorehead, S.M.; Watson, P.D.; Riner, W.; Bruke; J.R. Validity of the Computer Science and Applications (CSA) Activity Monitor in Children; *Med. Sci. Sports Exerc.* **1998**, *30*, 629-633.
29. Plasqui, G.; Joosen, A.M.; Kester, A.D.; Westerterp, K.R. Measuring Free Living Energy Expenditure and Physical Activity with Tri-Axial Accelerometry; *Obes. Res.* **2005**, *13*, 1363-1369.
30. Freedson, P.S.; Pober, D.; Janz, K.F. Calibration of Accelerometer Output for Children; *Med. Sci. Sports Exerc.* **2005**, *37*, S523-S530.
31. Freedson, P.; Miller, K. Objective Monitoring of Physical Activity Using Motion Sensors and Heart Rate; *Res. Q. Exerc. Sport.* **2000**, *71*, 21-29.
32. Kobayashi, S. *Nutrition Standards and Recommendations: Recent Trends in RDA, RDI and Dietary Guidelines and Their Background*; Kenpakusya: Tokyo, Japan, 1997; pp 86-96.
33. Kashiwazaki, H.; Dejima, Y.; Suzuki, T. Influence of Upper and Lower Thermoneutral Room Temperatures on Fasting and Post-Prandial Resting Metabolism under Different Outdoor Temperature; *Eur. J. Clin. Nutr.* **1990**, *44*, 405-413.
34. Yoshizawa, S. *Aerobic Capacity in Young Children*; Kyorin-Shoin: Tokyo, Japan, 2002; pp 61-71.
35. Yoshizawa, S.; Honda, H.; Urushihara, M. Nakamura, N. The Study on Aerobic Work Capacities of Preparatory School Children III. *Jpn. J. Phys Fitness Med.* **1981**, *30*, 73-85.
36. Hatano, Y.; Ono, M.; Miyazaki, Y. Heart Rate Response and Work Intensity on Treadmill Running in Preschool Children; *Rep. Res. Center Phys. Ed.* **1981**, *9*, 127-136.
37. Bland, J.M.; Altman, D.G. Statistical Methods for Assessing Agreement between Two Methods of Clinical Measurement; *Lancet* **1986**, *1*, 308-310.
38. *Human Energy Requirements. Report of a Joint FAO/WHO/UNU Expert Consultation*; Food and Nutrition Technical Report Series 1; U.N. Food and Agriculture Organization: Geneva, Switzerland, 2004; pp 35-52.
39. *Dietary Reference Values for Food Energy and Nutrients for the United Kingdom*; Report on Health and Social Subjects 41; 16th Impression; Department of Health; The Stationery Office: London, United Kingdom, 2007; pp 15-38.
40. Weir, J.B. New Methods for Calculating Metabolic Rate with Special Reference to Protein Metabolism; *J. Physiol.* **1949**, *109*, 1-9.
41. *The National Health and Nutrition Survey in Japan, 2003*; Ministry of Health, Labor, and Welfare of Japan: Tokyo, Japan, 2006; pp 318-319.
42. Honda, H.; Watanabe, N.; Ito, K.; Nakamura, N.; Yoshizawa, S. Changes in the Effects of 18 Month Endurance Run Training on Aerobic Work Capacity in Young Children; *Jpn. J. Phys. Fitness Med.* **1995**, *44*, 251-266.

43. Hendelman, D.; Miller, K.; Baggett, C.; Debold, E.; Freedson, P. Validity of Accelerometry for the Assessment of Moderate Intensity Physical Activity in the Field; *Med. Sci. Sports Exerc.* **2000**, *32*, S442-S449.
44. Tanaka, C.; Tanaka, S.; Kawahara, J.; Midorikawa, T. Triaxial Accelerometry for Assessment of Physical Activity in Young Children; *Obesity* **2007**, *15*, 1233-1244.
45. Debusk, R.F.; Valdez, R.; Houston, N.R.N.; Haskell, W. Cardiovascular Responses to Dynamic and Static Effort Soon after Myocardial Infarction; *Circulation* **1978**, *58*, 368-375.
46. Toner, M.M.; Sawka, M.N.; Levine, L.; Pandolf, K. Cardiorespiratory Responses to Exercise Distributed between the Upper and Lower Body; *J. Appl. Physiol.* **1983**, *54*, 1403-1407.
47. Vander, L.B.; Franklin, B.A.; Wrisley, D.; Rubenfire, M. Cardiorespiratory Responses to Arm and Leg Ergometry in Woman; *Phys. Sports Med.* **1984**, *12*, 101-106.
48. Hangerman, F.C.; Lawrence, R.A.; Mansfield, M.C. A Comparison of Energy Expenditure during Rowing and Cycling Ergometry; *Med. Sci. Sports Exerc.* **1988**, *20*, 479-488.
49. Pendergast, D.R. Cardiovascular; Respiratory, and Metabolic Responses to Upper Body Exercise; *Med. Sci. Sports Exerc.* **1989**, *21*, S121-S125.
50. *2005 NHK National Time Use Survey*; NHK Broadcasting Culture Research Institute: Tokyo, Japan, 2006; available at http://www.nhk.or.jp/bunken/book/book_data/bookdata_06020701.html (accessed April 19, 2010).
51. Hubal, E.A.C.; Sheldon, E.A.C.; Burke, J.M.; McCurdy, T.R.; Barry, M.R.; Rigas, M.L.; Zartarian, V.G.; Freeman, N.C.G. Children's Exposure Assessment: A Review of Factors Influencing Children's Exposure, and the Data Available to Characterize and Assess that Exposure; *Environ. Health Perspect.* **2000**, *108*, 475-486.
52. Kawahara, J.; Tanaka, C.; Tanaka, S.; Aoki, Y.; Yonemoto, J. Estimation of Daily Inhalation Rate of Preschool Children by Using Tri-Axial Accelerometer; *Epidemiology* **2008**, *19*, S139.
53. Lichtman, S.W.; Pisarska, K.; Berman, E.R.; Pestone, M.; Dowling, H.; Weisel, H.; Heshka, S.; Matthews, D.E.; Heymsfield, S.B. Discrepancy between Self-Reported and Actual Caloric Intake and Exercise in Obese Subjects; *New Engl. J. Med.* **1992**, *327*, 1893-1898.
54. *Methods for the Derivation of Inhalation Reference Concentrations and Application of Inhalation Dosimetry*; EPA/600/8-90/066F; U.S. Environmental Protection Agency: Washington, DC, 1994.
55. *Dietary Reference Intakes for Energy, Carbohydrate, Fiber, Fat, Fatty Acids, Cholesterol, Protein, and Amino Acids*; National Academy: Washington, DC, 2005; pp 880-935.

About the Authors

Dr. Junko Kawahara is a research fellow at the Research Center for Environmental Risk at the National Institute for Environmental Studies in Tsukuba, Ibaraki, Japan. Dr. Shigeho Tanaka is a project leader of the Project for Energy Metabolism on Health Promotion and Exercise Program of the National Institute of Health and Nutrition in Tokyo, Japan. Dr. Chiaki Tanaka is an associate professor in the Department of Health Science at the College of Health and Welfare of J.F. Oberlin University in Tokyo, Japan. Dr. Yuki Hikihara is a researcher in the Faculty of Engineering at Chiba Institute of Technology in Narashino, Japan. Dr. Yasunobu Aoki is General Manager of the Environmental Health Risk Research Section at the Research Center for Environmental Risk at the National Institute for Environmental Studies. Dr. Junko Yonemoto is Deputy Director of the Research Center for Environmental Risk at the National Institute for Environmental Studies. Please address correspondence to: Junko Kawahara, Research Center for Environmental Risk, National Institute for Environmental Studies, 16-2 Onogawa, Tsukuba, Ibaraki 305-8506, Japan; phone: +81-29-850-2695; fax: +81-29-850-2920; e-mail: jkawa@nies.go.jp.

Structural and Dynamic Features of the MutT Protein in the Recognition of Nucleotides with the Mutagenic 8-Oxoguanine Base*[S]

Teruya Nakamura[‡], Sachiko Meshitsuka[§], Seiju Kitagawa[§], Nanase Abe[§], Junichi Yamada[§], Tetsuya Ishino[§], Hiroaki Nakano[§], Teruhisa Tsuzuki[¶], Takefumi Doi[§], Yuji Kobayashi[§], Satoshi Fujii[∥], Mutsuo Sekiguchi**, and Yuriko Yamagata[‡1]

From the ‡Graduate School of Pharmaceutical Sciences, Kumamoto University, Kumamoto 862-0973, the §Graduate School of Pharmaceutical Sciences, Osaka University, Suita 565-0871, the ¶Graduate School of Medical Sciences, Kyushu University, Fukuoka 812-8582, the ∥School of Pharmaceutical Sciences, University of Shizuoka, Shizuoka 422-8526, and the **Fukuoka Dental College, Fukuoka 814-0193, Japan

Escherichia coli MutT hydrolyzes 8-oxo-dGTP to 8-oxo-dGMP, an event that can prevent the misincorporation of 8-oxoguanine opposite adenine in DNA. Of the several enzymes that recognize 8-oxoguanine, MutT exhibits high substrate specificity for 8-oxoguanine nucleotides; however, the structural basis for this specificity is unknown. The crystal structures of MutT in the apo and holo forms and in the binary and ternary forms complexed with the product 8-oxo-dGMP and 8-oxo-dGMP plus Mn^{2+}, respectively, were determined. MutT strictly recognizes the overall conformation of 8-oxo-dGMP through a number of hydrogen bonds. This recognition mode revealed that 8-oxoguanine nucleotides are discriminated from guanine nucleotides by not only the hydrogen bond between the N7-H and Oδ (N119) atoms but also by the *syn* glycosidic conformation that 8-oxoguanine nucleotides prefer. Nevertheless, these discrimination factors cannot by themselves explain the roughly 34,000-fold difference between the affinity of MutT for 8-oxo-dGMP and dGMP. When the binary complex of MutT with 8-oxo-dGMP is compared with the ligand-free form, ordering and considerable movement of the flexible loops surrounding 8-oxo-dGMP in the binary complex are observed. These results indicate that MutT specifically recognizes 8-oxoguanine nucleotides by the ligand-induced conformational change.

Although spontaneous mutations are indispensable to the evolutionary process of living organisms, they can also be lethal to the organism. Among the various modified bases in DNA,

RNA, and nucleotides, 8-oxoguanine (8-oxoG),[2] a damaged form of guanine (G) generated by reactive oxygen species, is known to have highly mutagenic potency because of its mispairing with adenine. Therefore, organisms have an error avoidance pathway for preventing mutations caused by 8-oxoG. The *Escherichia coli* MutT protein (129 amino acids, $M_r = 14,900$) hydrolyzes 8-oxo-dGTP and 8-oxo-GTP to their corresponding nucleoside monophosphates and inorganic pyrophosphate in the presence of Mg^{2+} (1, 2). Because 8-oxo-dGTP and 8-oxo-GTP can be misincorporated opposite adenine by DNA and RNA polymerases, the hydrolysis of the damaged nucleotides by MutT can avoid replicational and transcriptional errors. In DNA, 8-oxoG paired with cytosine is excised by MutM, an 8-oxoG DNA glycosylase, whereas MutY, an adenine DNA glycosylase, removes adenine paired with 8-oxoG (3–6).

The substrate specificities of enzymes that recognize 8-oxoG are quite varied. MutT exhibits high substrate specificity for 8-oxoG nucleotides; that is, the K_m for 8-oxo-dGTP is 14,000-fold lower than that for dGTP (7). In contrast, human MutT homologue 1 (hMTH1) hydrolyzes not only 8-oxo-dGTP but also several oxidized purine nucleotides such as 2-oxo-dATP, 2-oxo-ATP, 8-oxo-dATP, and 8-oxo-ATP. In terms of the hydrolysis of 8-oxo-dGTP, the K_m of hMTH1 for 8-oxo-dGTP is only 17-fold lower than that for dGTP (8, 9). The solution structure of hMTH1 as determined by NMR has revealed its overall architecture and possible substrate-binding region (10); however, the broad substrate recognition mechanism of hMTH1 remains to be elucidated. MutM and MutY also have low specificity for 8-oxoG. For example, MutM can recognize a variety of damaged bases such as formamidopyrimidine, 5-hydroxycytosine, and dihydrouracil in addition to 8-oxoG (11–13), and MutY shows a kinetic preference for A:8-oxoG that is only 6-fold greater than that for A:G (14).

The crystal structures of OGG1, MutM, and MutY complexed with 8-oxoG-containing DNA (13, 15, 16) have revealed

[2] The abbreviations used are: 8-oxoG, 8-oxoguanine; Nudix, nucleoside diphosphate linked to some other moiety, X; SLHL, strand-loop-helix-loop; r.m.s.d., root mean square deviation; AMPCPP, adenosine 5′-(α,β-methylenetriphosphate); SeMet, selenomethionine; hMTH1, human MutT homologue 1.

that, interestingly, OGG1 and MutM do not recognize the O8 atom, which is the most characteristic feature of the 8-oxoG moiety, and the interaction observed between the O8 atom and the main-chain atom of MutY is relatively weak. Alternatively, OGG1, MutM, and MutY commonly discriminate 8-oxoG from G by the protonation at N7 accompanied by the oxidation of C8. Structural studies on various enzymes that recognize 8-oxoG have succeeded in explaining the mechanism by which 8-oxoG is discriminated from normal G in DNA, but one of the most interesting questions to be elucidated is the mechanism by which MutT acquires extremely high substrate specificity for 8-oxoG compared with the other enzymes.

MutT belongs to the Nudix (nucleoside diphosphate linked to some other moiety, X) hydrolase family (17). Nudix family members have a highly conserved MutT signature (Nudix motif); *i.e.* GX$_5$EX$_7$REUX*EE*XGU, where U is a hydrophobic residue and *X* is any amino acid. Current genome analyses have found a large number of open reading frames containing the MutT signature, but their functions, *i.e.* their substrates, are not identified in the case of almost all these proteins because of a lack of homology outside the MutT signature. MutT is the most examined protein in this family. Its structure was first determined by NMR (18) and has greatly contributed to the study of the Nudix hydrolase family. NMR studies of MutT with its product, 8-oxo-dGMP, have predicted several recognition models of 8-oxo-dGMP (19). However, the precise recognition mechanism of 8-oxoG nucleotides remains unclear. Therefore, it is necessary to determine the crystal structures of MutT to explain the extremely high substrate specificity of MutT for 8-oxoG nucleotides.

Here, we present x-ray crystallographic analyses of the apo enzyme; the Mn^{2+}-bound holo enzyme (MutT-Mn^{2+}); the binary complex with 8-oxo-dGMP, a reaction product (MutT-8-oxo-dGMP); and the tertiary complex with 8-oxo-dGMP and Mn^{2+} (MutT-8-oxo-dGMP-Mn^{2+}). These structures have revealed the mechanism of the extremely high substrate specificity of MutT for 8-oxoG nucleotides and have allowed us to propose the exact roles of some conserved residues in the MutT signature.

EXPERIMENTAL PROCEDURES

Protein Expression and Purification—The *E. coli* strain BL21 (DE3) harboring a newly constructed pET8c/MutT plasmid was used for the expression of native and selenomethionine (SeMet)-substituted MutTs. Native MutT was overexpressed in Luria-Bertani (LB) broth, and SeMet MutT was overexpressed in LeMaster broth containing seleno-DL-methionine instead of methionine with sufficient amounts of isoleucine, lysine, and threonine to inhibit the methionine pathway (20, 21). This condition was also present in the overexpression of SeMet hMTH1 (22). Purification of MutT was carried out by almost the same procedure (except that the hydroxyapatite column chromatography step was skipped), as described previously (23). DEAE-Sepharose and the HiPrep 16/60 Sephacryl S-200 HR column were substituted for DEAE-Sephacel and the Sephadex G-75 column, respectively. The purified protein solution was concentrated to ~6 mg/ml.

Crystallization—The native and SeMet-substituted apo forms and all complexes were crystallized by hanging drop vapor diffusion at 288 K. Crystals of native and SeMet-substituted forms were obtained from a droplet containing 3 mg/ml protein, 10 mM Tris-HCl (pH 7.5), 0.5 mM EDTA, 2.5% glycerol, 0.5 mM 2-mercaptoethanol, 0.7 M potassium sodium tartrate, and 44 mM HEPES-NaOH (pH 7.5) equilibrated against a reservoir containing 1.4 M potassium sodium tartrate and 87 mM HEPES-NaOH (pH 7.5). Crystals of MutT-Mn^{2+} were obtained in the same manner, as described above, except that 10 mM MnCl$_2$ was added to the droplet. The crystallizations of MutT-8-oxo-dGMP and MutT-8-oxo-dGMP-Mn^{2+} were described previously (24). The crystals were transferred to a cryosolution of each reservoir containing 30% sucrose and were then flash frozen.

Data Collection, Processing, Phasing, and Structure Refinement—Diffraction data were collected at 100 K on beam-line 18B of the Photon Factory (Tsukuba, Japan) and on beam-lines 41XU, 44XU, 38B1, and 40B2 of SPring-8 (Harima, Japan). The data for native and SeMet derivative forms were processed and scaled by DSP/MOSFLM and SCALA (25). The data for MutT-Mn^{2+} were processed and scaled by DENZO and SCALEPACK (26). There are two molecules in the asymmetric unit with V_M of 2.2 (native MutT) and 2.5 (MutT-Mn^{2+}) Å^3·Da^{-1} (27). Data collection statistics of the best data used for structure determination and refinements are listed in Table 1. Data collection statistics of MutT-8-oxo-dGMP and MutT-8-oxo-dGMP-Mn^{2+} are quoted from the reference by Nakamura *et al.* (24).

The positions of eight selenium atoms were determined using SOLVE (28). The initial phases were calculated using MLPHARE (29) and improved using DM (30). The initial model was built using TOM (31) and O (32). The model was refined using X-PLOR (33) and CNS (34). Using the model of the SeMet derivative, the successive refinement of native MutT converged at an R value of 20.4% and an R_{free} of 23.1% for reflections in the resolution range 20–1.8 Å. The structure of MutT-8-oxo-dGMP was solved by molecular replacement with AMoRe (35) using the structure of the native apo form as a search model. The $2F_o - F_c$ maps after CNS refinements clearly showed the density for 8-oxo-dGMP and the conformationally changed loop regions (L-A and L-D). These regions were manually built and fitted into the density with O. The structure of MutT-8-oxo-dGMP-Mn^{2+} was refined starting with the coordinates of the MutT-8-oxo-dGMP. The structure of MutT-Mn^{2+} was solved by molecular replacement with AMoRe by using the structure of the apo form as a search model. The stereochemical qualities of the structures were checked by PROCHECK (36); the refinement statistics are listed in Table 2. Superposition of MutT structures were carried out using Lsqkab (37). All molecular graphics were prepared using PyMOL (38).

RESULTS AND DISCUSSION

Overall Structures of MutT and MutT-8-oxo-dGMP—The crystal structures of the MutT apo and MutT-8-oxo-dGMP complex forms were determined at a resolution of 1.8 and 1.96 Å, respectively. MutT is composed of two α-helices (α-1 and α-2) and six β-strands (β-1 to β-6) (Figs. 1 and 2*A*); it adopts an

TABLE 1

Data collection statistics

Values in parentheses correspond to the highest resolution shell.

Diffraction data	MutT				MutT–8-oxo-dGMP	MutT–8-oxo-dGMP–Mn²⁺
	Native	Peak	Edge	Remote		
Beam line	SPring-8 BL41XU		PF BL18B		SPring-8 BL41XU	SPring-8 BL40B2
Wavelength (Å)	0.7080	0.9793	0.9791	0.9500	0.9000	1.296
Space group	$P2_1$		$P2_1$		$P2_12_12_1$	$P2_12_12_1$
Unit-cell lengths (Å, °)	$a = 33.9$		$a = 34.1$		$a = 37.9$	$a = 38.2$
	$b = 71.6$		$b = 71.1$		$b = 56.0$	$b = 56.0$
	$c = 55.8$		$c = 55.7$		$c = 59.4$	$c = 59.3$
	$\beta = 99.0$		$\beta = 98.7$			
Resolution range (Å)	20.0–1.8 (1.9–1.8)		20.0–2.2 (2.3–2.2)		20.0–1.96 (2.08–1.96)	18.56–2.56 (2.72–2.56)
No. of observed reflections	85,618	49,308	49,226	50,094	54,195	26,502
No. of unique reflections	24,217	13,041	13,015	13,147	9,344	4,395
Completeness (%)	99.7 (99.7)	97.2 (97.2)	97.3 (97.3)	98.3 (98.3)	97.6 (93.2)	99.2 (95.7)
$R_{\mathrm{merge}}{}^a$ (%)	3.1 (9.4)	3.9 (12.1)	3.8 (12.3)	3.9 (12.1)	6.5 (18.1)	7.7 (15.2)
$\langle I/\sigma \rangle$	15.8 (7.9)	8.8 (3.3)	9.4 (5.0)	8.8 (5.6)	29.6 (6.2)	45.9 (22.6)

	MutT-Mn²⁺
Beam line	PF BL18B
Wavelength (Å)	1.000
Space group	$P2_1$
Unit-cell lengths (Å, °)	$a = 35.8$
	$b = 56.0$
	$c = 74.1$
	$\beta = 96.4$
Resolution range (Å)	40.0–2.0 (2.03–2.00)
No. of observed reflections	77,213
No. of unique reflections	19,810
Completeness (%)	98.1 (96.2)
$R_{\mathrm{merge}}{}^a$ (%)	4.2 (6.4)
$\langle I/\sigma \rangle$	28.6 (18.6)

$^a R_{\mathrm{merge}} = 100 \times \Sigma |I_{\mathrm{hkl}} - \langle I_{\mathrm{hkl}} \rangle| / \Sigma I_{\mathrm{hkl}}$, $\langle I_{\mathrm{hkl}} \rangle$ is the mean value of I_{hkl}.

TABLE 2

Refinement statistics

Diffraction data	MutT	MutT–8-oxo-dGMP	MutT–8-oxo-dGMP–Mn²⁺	MutT-Mn²⁺
Resolution range (Å)	20.0–1.8	20.0–1.96	18.56–2.56	20.0–2.0
Number of reflections used	24,213	9,280	4,394	19,386
Number of atoms				
Protein	2,025	1,038	1,029	2,010
Water	190	136	92	131
Nucleotide	0	24	24	0
Mn²⁺ ion	0	0	1	4^a
Other	11	34	5	32
Completeness (%)	99.1	97.3	99.9	98.1
$R_{\mathrm{cryst}}/R_{\mathrm{free}}{}^b$ (%)	20.4/23.1	17.8/20.1	19.3/24.2	19.2/22.7
Ramachandran plot (%)				
Most favored	93.0	91.5	87.6	94.9
Additional allowed	7.0	8.5	12.4	5.1
Generously allowed	0	0	0	0
Disallowed	0	0	0	0
r.m.s.d. in bonds (Å)	0.005	0.005	0.007	0.005
r.m.s.d. in angles (°)	1.2	1.3	1.3	1.2

^{a} Two ions per monomer.

$^b R_{\mathrm{cryst}} = 100 \times \Sigma \|F_o| - |F_c\| / \Sigma |F_o|$. R_{free} was calculated from the test set (5% of the total data).

α-β-α sandwich structure that is conserved among members of the Nudix family. The Nudix motif (23 residues from Gly-38 *i.e.* the MutT signature (GX₅EX₇REUXEEXGU), adopts the characteristic strand-loop-helix-loop (SLHL) structure formed by β-3′, L-B, α-1, and L-C (39, 40). The crystal of the apo form contains two protein molecules per asymmetric unit, and they are very similar to each other with root mean square deviation (r.m.s.d.) of 0.5 Å for the corresponding 121 Cα atoms. For simplicity, only one molecule will be referred to in all further discussions. MutT exists as a monomer, which is found in the MutT-8-oxo-dGMP crystal.

In the apo form, the electron densities of L-A connecting β-2 and β-3 are not available, indicating that the L-A loop region has a highly flexible conformation (Fig. 2A). On the other hand, in the MutT-8-oxo-dGMP complex, the ordering of the flexible

L-A loop by interactions with 8-oxo-dGMP was observed (Fig. 2, *B* and *C*). The plot of the displacement between the Cα atoms of the apo and complex forms is shown in supplemental Fig. S1A. The movements of the L-A and L-D regions are large (~8–10 Å) (Fig. 2C and supplemental Fig. S1A). Except for these loop regions, the two forms have a similar structure with an r.m.s.d. of 0.9 Å for the corresponding 101 Cα atoms.

A structural similarity search performed using the DALI server (41), with the coordinates of MutT-8-oxo-dGMP, indicated that 62 proteins (154 Protein Data Bank (PDB) ID numbers, 278 protein chains) are structural homologs of MutT with Z-scores of >6.0 and belong to the Nudix superfamily with the Nudix fold. The MutT structure, with two α-helices and six β-strands, comprises the smallest structural unit among members of the Nudix superfamily. Of 62 proteins, half have
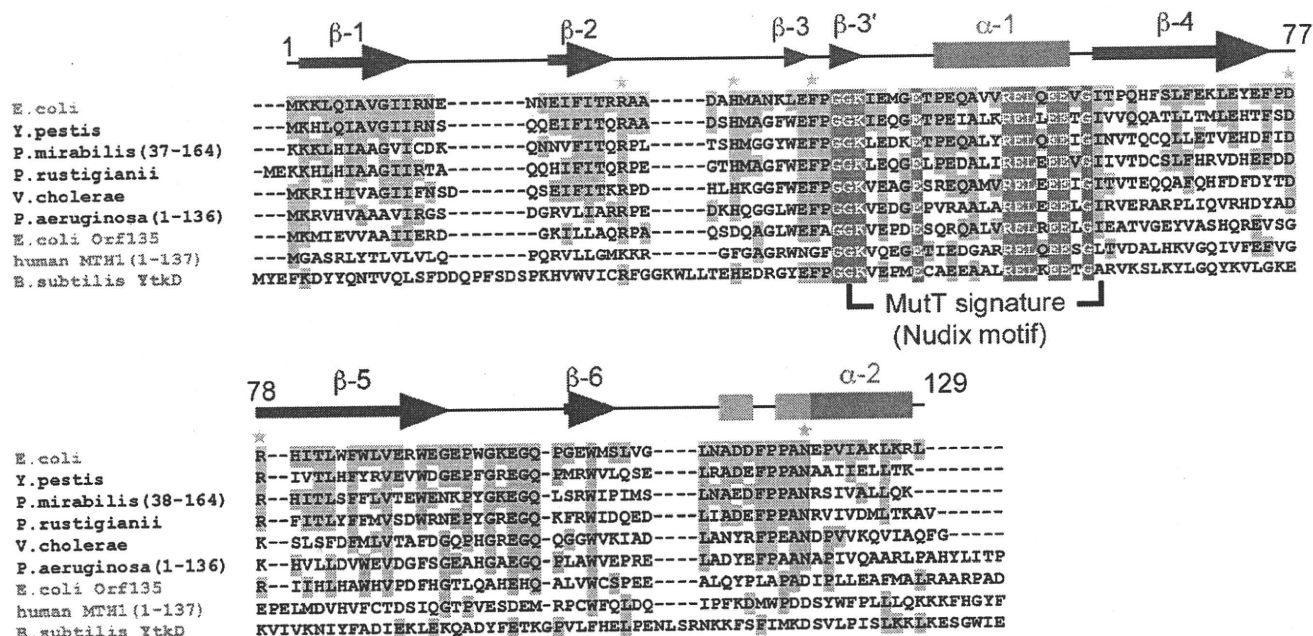
FIGURE 1. **Sequence alignment of MutT family proteins.** Amino acid sequences of MutT family proteins were aligned using ClustalW (72). MutT homologs from species related to *E. coli*, which share high sequence similarity, were chosen and are listed. They are from *E. coli* (CAA28523), *Yersinia pestis* (NP_670913), *Proteus mirabilis* (ZP_03840798), *Providencia rustigianii* (ZP_03315124), *Vibrio cholerae* (NP_232022), and *Pseudomonas aeruginosa* (ZP_04932260). In addition to *E. coli* MutT, *E. coli* Orf135 (BAA15549), human MTH1 (BAA07601), and *B. subtilis* YtkD (NP_390941), which have 8-oxo-dGTPase activity *in vitro*, were added and are shown in *red*. Absolutely conserved residues are shown in *red*, and identical residues are in *pink*. The *green asterisks* on the *E. coli* MutT sequence indicate amino residues that participate in the recognition of 8-oxoG and the ligand-induced conformational change. The secondary structure of *E. coli* MutT in the apo form is shown at the *top*. The α-helices, β-strands, and 3_{10} helices are represented as *red bars*, *blue arrows*, and *pink bars*, respectively.

unknown functions. Structures that are highly similar to the MutT complex form are the monomer structures of *Bdellovibrio bacteriovorus* RNA pyrophosphohydrolase; *i.e.* BdRppH in the ternary and binary forms complexed with GTP and Mg^{2+} (BdRppH-GTP-Mg^{2+}, 3FFU, r.m.s.d. = 1.8 Å, Z = 19.0) and with dGTP (BdRppH-dGTP, 3EF5, r.m.s.d. = 1.9 Å, Z = 18.3) (40) and unknown proteins from *Bartonella henselae* (3HHJ, r.m.s.d. = 1.8 Å, Z = 19.8) and *Methanosarcina mazei* (3GRN, r.m.s.d. = 2.1 Å, Z = 17.5), respectively. In MutT, the r.m.s.d. is rather large: 3.3 Å for 120 Cα atoms between the x-ray and NMR structures in the ligand-free form and 3.5 Å for 127 Cα atoms between structures in the complex form (PDB IDs: 1MUT and 1PUS) (18, 19).

Recognition Scheme of 8-oxo-dGMP by MutT—When 8-oxo-dGMP binds to MutT, large ligand-induced conformational changes occur in the L-A and L-D regions, namely, the ordering of the flexible L-A loop and considerable movement of L-A and L-D to the surrounding 8-oxo-dGMP (Figs. 2C and 3A). The side chains of Arg-23 and His-28 on L-A form hydrogen-bonding interactions with phosphate and sugar moieties of 8-oxo-dGMP, respectively, whereas Arg-78 interacts with the sugar moiety through a water-mediated hydrogen bond. Asp-77 and Arg-78 make two hydrogen bonds between their side chains. The conformational change of the L-A and L-D regions also produces the water molecule-mediated interaction between His-28 and Asp-77 and the CH-π interaction between His-28 and Phe-75 (Fig. 3A and supplemental Fig. S2). Thus, the loops L-A and L-D connect to each other, resulting in the formation of a cave composed of β-1, β-3, β-3′, β-5, and α-2 for substrate binding (Fig. 3B). 8-Oxo-dGMP is inserted deeply into the cave

in which the wall on one side is filled with hydrophobic residues (Leu-4, Ile-6, Val-8, Ile-80, and Leu-82), and the other side and bottom include some polar residues (Arg-23 and Asn-119). The 8-oxoG base and the deoxyribose are perfectly buried, and the phosphate group faces the solvents (Fig. 3B). The glycosidic conformation of 8-oxo-dGMP bound to MutT is *syn*. This fact is consistent with the first suggestion by Bessman *et al.* that MutT may recognize the *syn* conformation, because the 8-substituted purine nucleotides were better substrates compared with the normal purine nucleotides (42). The sugar ring puckering and the sugar-phosphate backbone conformation of 8-oxo-dGMP are C2′-*endo* and *gauche⁻-trans*, respectively. These conformations are generally observed in 8-substituted purine nucleosides and 5′-nucleotides (43).

These ligand-induced conformational changes result in the strict recognition of the overall structure of 8-oxo-dGMP by MutT through a number of hydrogen bonds (Fig. 3C). The characteristic features of the 8-oxoG base are the oxygen atom (O8) at C8 and the hydrogen atom (N7-H) at N7 accompanied by oxidation. MutT recognizes N7-H of 8-oxoG by a hydrogen bond with Oδ of Asn-119 (Fig. 3C, a *red dashed line*). The 8-oxoG base is also recognized by hydrogen bonds with Asn-119 and Phe-35; *i.e.* the Nδ of Asn-119 forms a hydrogen bond with O6 of 8-oxoG, and the main-chain atoms of Phe-35 participate in three types of hydrogen bonds with N2-H, N1-H, and O6. On the other hand, the O8 atom does not form hydrogen bonds with any amino acid residues, although it does participate in the weak C-H–O interaction with the phenyl ring C-H of Phe-75 (C–O distance, 3.4 Å) and the van der Waals interactions with the side-chain C-H moieties of Phe-75, Pro-116, Leu-
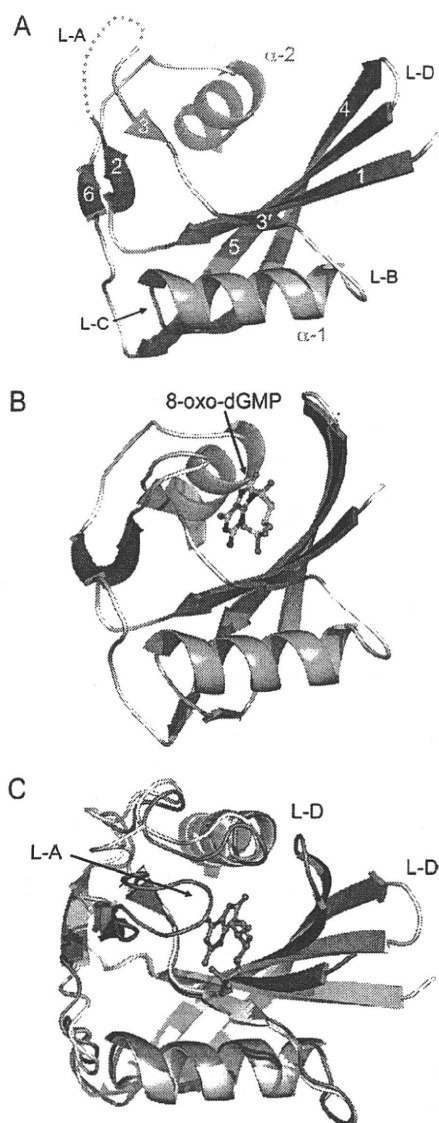
FIGURE 2. **Crystal structures of MutT apo and MutT-8-oxo-dGMP complex forms.** *A,* overall structure of MutT. α-Helices are in *pink,* and β-strands are in *slate.* A missing region of L-A is shown as a *gray dashed line. B,* overall structure of MutT-8-oxo-dGMP. 8-Oxo-dGMP is shown in *ball and stick representation. C,* comparison of the structures of the apo and complex forms. Apo and complex forms are shown in *gray* and *slate,* respectively. L-A and L-D regions in MutT-8-oxo-dGMP adopt a closed conformation as compared with those in the apo form.

82, Ile-80, and Ala-118 (Fig. 3*D*). In addition, the carbonyl oxygen of Gly-37 forms water molecule-mediated hydrogen bonds with N2-H of 8-oxoG and the phosphate oxygen. The side chain of His-28 is directly hydrogen-bonded to the O3′ atom of the deoxyribose. The O3′ atom also forms a hydrogen bond with a water molecule, binding to the side chain of Arg-78. The phosphate group forms a hydrogen bond with the side chain of Arg-23 and a water molecule-mediated hydrogen bond with the main chain of Lys-39. In summary, 8-oxo-dGMP is surrounded by 12 types of hydrogen bonds. The hydrogen-bonding interactions with the pyrimidine moiety and the α-phosphate group in MutT-8-oxo-dGMP are similar to those with the corresponding pyrimidine moieties and α-phosphate groups in the structures of BdRppH-GTP-Mg^{2+} and BdRppH-dGTP (BdRppH-

(d)GTPs) (40). The positions of the base moieties of (d)GTPs with the *syn* conformation in BdRppH-(d)GTPs accord with that of 8-oxo-dGMP in MutT-8-oxo-dGMP with an r.m.s.d. of 0.6 Å for the corresponding 11 atoms when proteins are superimposed. BdRppH with Arg-40, Phe-52, and Asn-136 residues corresponding to Arg-23, Phe-35, and Asn-119 of MutT, respectively, recognizes N1-H, N2-H, and O6 of the pyrimidine moiety by four hydrogen bonds with Phe-52 and Asn-136; Pα-O of the α-phosphate group is recognized by a hydrogen bond with Arg-40. This recognition mode is the same as that observed in MutT. Apart from the similarities, differences are found in recognition of the imidazole moiety of the base and the sugar moiety as well as in the ligand-induced conformational change. The imidazole and sugar moieties of (d)GTPs in BdRppH-(d)GTPs do not form hydrogen bonds with any residues in BdRppH. In addition, although ligand-induced conformational change with loop ordering is observed in BdRppH, the change is significantly small (~2–4 Å) as compared with that in MutT. The large ligand-induced conformational change observed in MutT does contribute to its high affinity for 8-oxoG nucleotides, as discussed below. There is a large discrepancy between the K_m values of 0.081 and 268 μM for the hydrolysis of 8-oxo-dGTP by MutT and of dGTP by BdRppH, respectively (7, 44). This may derive from these structural differences, in addition to the unfavorable *syn* conformation of (d)GTPs in BdRppH-(d)GTPs.

As a result of the strict recognition of 8-oxo-dGMP with the large conformational change, there are low *B* factors and unambiguous electron densities around 8-oxo-dGMP (supplemental Fig. S1*B* and Fig. 3*E*). The average *B* factor of 8-oxo-dGMP is 12.4 $Å^2$ and that of the residues involved in the recognition of 8-oxo-dGMP, Arg-23, His-28, Phe-35, Asp-77, Arg-78, and Asn-119 is 13.6 $Å^2$. These low *B* factors and unambiguous electron densities represent the small thermal motion and/or the ordered positioning of 8-oxo-dGMP and the residues of the active site in the crystal lattice. This phenomenon explains isothermal titration calorimetry experiments (45), indicating that the tight binding of 8-oxo-dGMP to MutT ($\Delta G = -9.8$ kcal/mol) is driven by a highly favorable enthalpy ($\Delta H = -39.0$ kcal/mol) with an unfavorable entropy ($-T\Delta S = 29.2$ kcal/mol). The unfavorable entropy would be a result of the conformational rigidity generated from the connection of loops L-A and L-D with large ligand-induced conformational changes. On the other hand, the more favorable enthalpy would be produced by the large number of hydrogen bonds and van der Waals interactions formed between 8-oxo-dGMP and MutT; this is sufficient to compensate for the unfavorable entropy and to bind tightly.

Furthermore, the hydrogen bond-mediated recognition mode found in MutT-8oxo-dGMP is comparable with the results of mutational studies in which it was found that the R78A, N119D, and N119A mutants show 7-, 37-, and 1650-fold decreases in affinity for 8-oxo-dGMP in comparison with the wild type and that they lose binding free energies ($\Delta\Delta G$) of 1.1, 2.1, and 4.3 kcal/mol, respectively, as measured by the increases in K_I (46). According to previous reports, the contribution of the hydrogen bond to protein stability can be estimated as ~2 and 1.2 kcal/mol for hydrogen bonds between protein residues
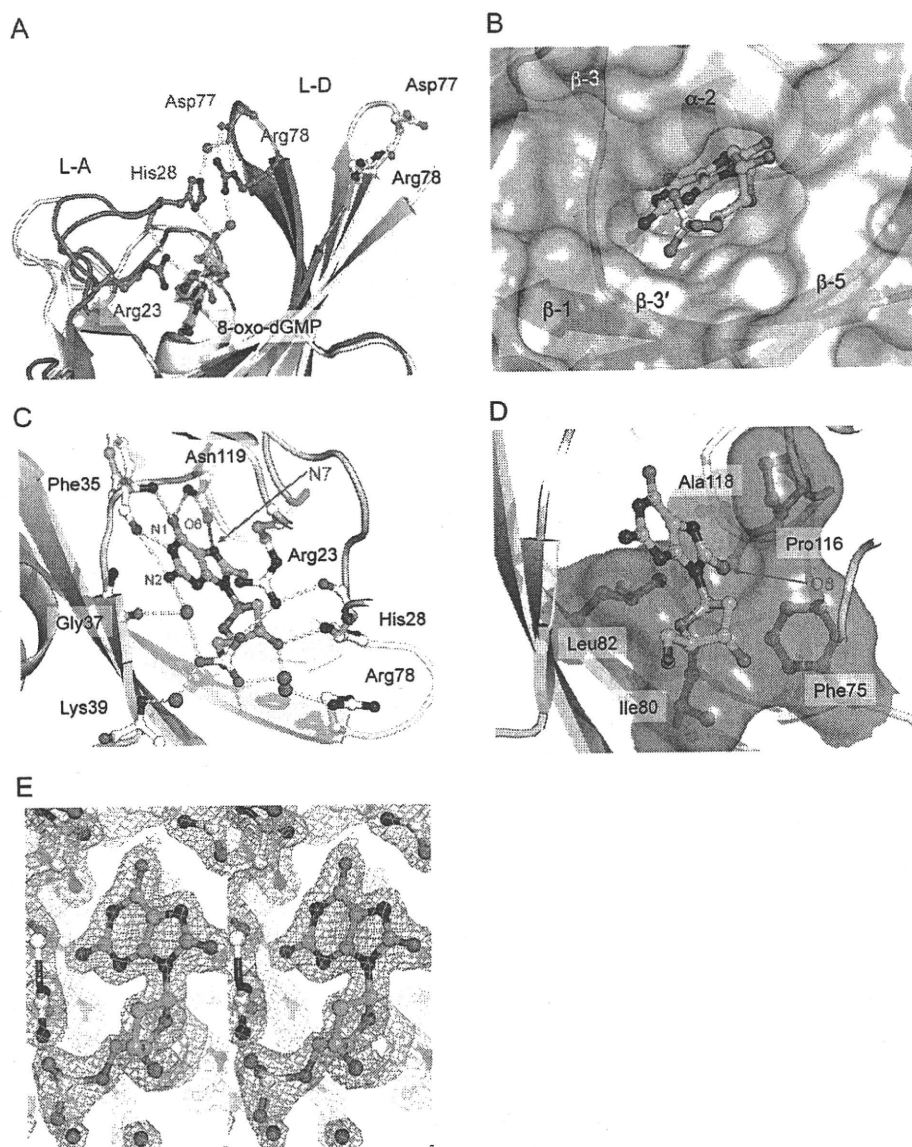
FIGURE 3. **Recognition of 8-oxo-dGMP by MutT.** *A*, hydrogen bonding interactions between 8-oxo-dGMP and loop regions (apo in *gray* and MutT-8-oxo-dGMP in *slate*). Amino acid residues involved in the hydrogen bonding interactions are shown in *ball and stick representation*. Water molecules are in *red*. Hydrogen bonds are shown as *yellow dashed lines*. *B*, the hydrophobic cave composed of β-1, β-3, β-3′, β-5, and α-2 is represented as a *translucent surface* (carbon in *white*, nitrogen in *cyan*, and oxygen in *pink*). *C*, interactions for the *syn* conformation of 8-oxo-dGMP. The hydrogen bond between Oδ of Asn-119 and N7-H of 8-oxoG is shown as a *red dashed line*. *D*, van der Waals interactions around the O8 atom. Amino acid residues recognizing O8 are shown in *ball, stick*, and *translucent surface*. *E*, a $2F_o - F_c$ electron density map around 8-oxo-dGMP contoured at 1.5 σ (*stereo view*).

both deoxyribose and ribose derivatives of 8-oxoG nucleotides with similar efficiency (2, 7). This is because, despite a number of hydrogen-bonding interactions between 8-oxo-dGMP and MutT, there is space for a hydroxyl group instead of the hydrogen atom at the 2′ position of the sugar ring (Fig. 3*B*). This recognition mechanism of 8-oxo-dGMP by MutT is different from any models predicted by NMR studies (PDB IDs: 1PPX, 1PUN, 1PUQ, 1PUS, and 1MUT) (supplemental Fig. S3).

Discrimination of 8-oxoG Nucleotides from G Nucleotides—The K_m values of *E. coli* MutT for 8-oxo-dGTP and 8-oxo-GTP are ~3,800- to 14,000-fold lower than the values for the corresponding G nucleotides (7). These data agree with the observation that the K_d value (52 nM) between 8-oxo-dGMP and MutT is 34,000-fold lower than that (1.76 mM) between dGMP and MutT (45). Thus, the most important question that this study addresses is the mechanism by which MutT obtains high substrate specificity for 8-oxoG nucleotides as compared with G nucleotides.

According to the recognition scheme of 8-oxo-dGMP by MutT, the major difference in the recognition of 8-oxoG *versus* G is whether the single hydrogen bond between Oδ of Asn-119 and N7-H of 8-oxoG occurs or not. This situation is similar to those of OGG1, MutM, and MutY (13, 15, 16). If the side-chain conformation of Asn-119 in the MutT complex with G nucleotides was the same as that in the MutT-8-oxo-dGMP structure, the two lone pairs at N7 of G and Oδ of Asn-119

would be repulsive (supplemental Fig. S4). To avoid this repulsion, a rotation about the side-chain torsion angles in Asn-119 should be required. Thus, the difference in the number of hydrogen bonds formed between MutT-G and MutT-8-oxoG complexes is only one. The contribution of one hydrogen bond to ΔΔG is estimated to be 2 kcal/mol (47, 48).

The *syn* glycosidic conformation of 8-oxo-dGMP must also be one of the elements contributing to the substrate specificity of MutT, because 8-oxoG nucleotides favor a *syn* conformation by the steric hindrance between O8 and the sugar moiety; this is in contrast with G nucleotides that adopt both *syn* and *anti* conformations (49, 50). Because of the lack of quantitative data

and for those between a water molecule and a protein residue, respectively (47, 48). Judging from the MutT-8oxo-dGMP structure, the N119D and N119A mutants lose one hydrogen bond between the O6 of 8-oxo-dGMP and the Nδ-H of Asn-119 and two hydrogen bonds involving the O6 and N7-H of 8-oxo-dGMP and the amide group of Asn-119, respectively (Fig. 3*C*). The R78A mutant loses the hydrogen bond to a water molecule (Fig. 3*C*); that is, ΔΔG losses of 1.2, 2, and 4 kcal/mol are estimated for the R78A, N119D, and N119A mutants, respectively; this agrees perfectly with the experimental data (46).

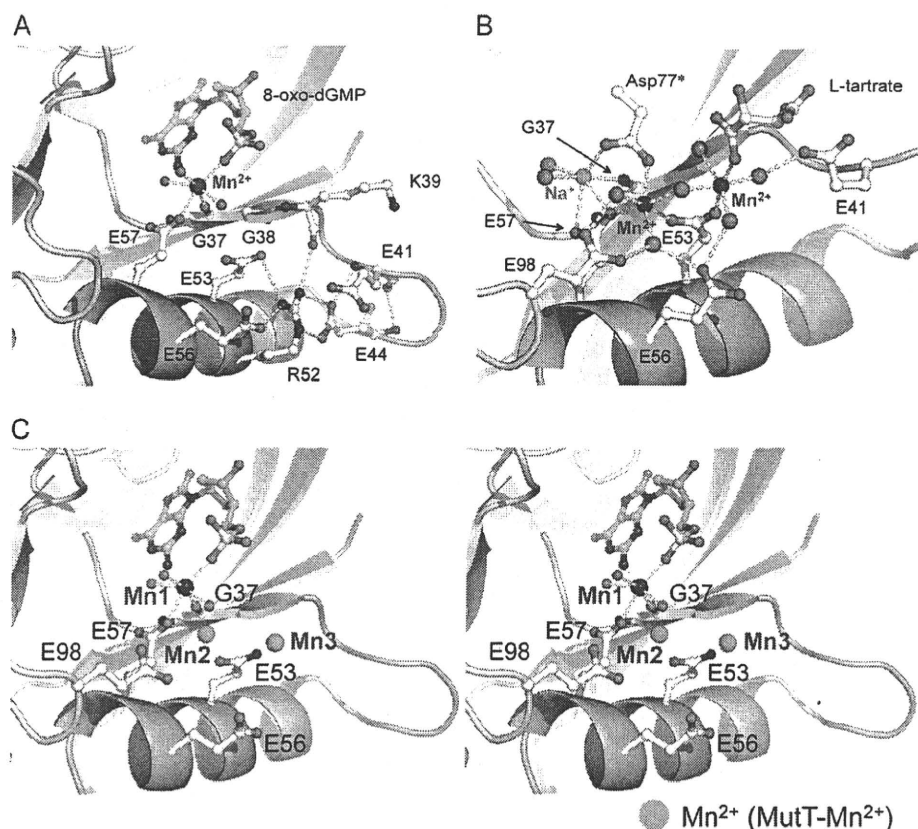The feature of the substrate-binding site in MutT-8-oxo-dGMP is also consistent with reports that MutT hydrolyzes

FIGURE 4. **Coordination scheme of Mn²⁺ at the MutT signature in MutT-8-oxo-dGMP-Mn²⁺ and MutT-Mn²⁺.** *A*, the coordination scheme of Mn²⁺ and the structure of the MutT signature in MutT-8-oxo-dGMP-Mn²⁺. Mn²⁺ in *blue* has an ideal octahedral coordination with Gly-37, Glu-57, Pα-O of 8-oxo-dGMP, and water molecules. The hydrogen bonding interactions shown in *yellow dashed lines* contribute to the conformational stabilization of the SLHL structure of the MutT signature. The SLHL structure is in *pink*. *B*, the coordination scheme of Mn²⁺ in MutT-Mn²⁺. Na⁺ is shown in *green*. Asp-77* is an amino acid of another molecule in the asymmetric unit. *C*, superposition of two Mn²⁺ ions in MutT-Mn²⁺ onto the structure of MutT-8-oxo-dGMP-Mn²⁺ (*stereo view*). *Coloring* is as in *A*. Mn²⁺ ions observed in MutT-Mn²⁺ are shown in *cyan* (Mn2 and Mn3).

on the preference of the *syn* conformation about the 8-oxoG nucleotides, it is difficult to estimate the free energy difference between the *syn* and *anti* conformations. However, it is unlikely that the preference of MutT for the *syn* conformation over the *anti* conformation is more than 10-fold ($\Delta\Delta G \approx 1.4$ kcal/mol), because the *anti* conformation for 8-oxoG nucleotides is sometimes observed in the crystal structures of 8-oxoG recognition complexes such as OGG1 and MutY (15, 16).

These discrimination factors cannot by themselves explain the roughly 34,000-fold difference between the binding affinity of MutT for 8-oxo-dGMP and dGMP ($\Delta\Delta G \approx 6$ kcal/mol). When 8-oxo-dGMP binds to MutT, large ligand-induced conformational changes with an ordering of loop regions are observed. On the other hand, in the binding of dGMP to MutT, the thermal parameters were $\Delta G = -3.7$, $\Delta H = -3.3$, and $-T\Delta S = -0.4$ kcal/mol; the changes in backbone ¹⁵N and NH chemical shifts in 22 residues; and the slowing down of the NH exchange with D_2O of 20 residues are remarkably different when compared with the changes (the thermal parameters of $\Delta G = -9.8$, $\Delta H = -39.0$, and $-T\Delta S = 29.2$ kcal/mol; the changes in backbone ¹⁵N and NH chemical shifts in 62 residues; and the slowing down of the NH exchange with D_2O of 45 residues) involved in the binding of 8-oxo-dGMP to MutT (19,

45). These facts suggest that no significant conformational change in MutT is observed when dGMP binds to MutT. The large ligand-induced conformational change in MutT also contributes to the discrimination of 8-oxoG nucleotides from G nucleotides.

A comparison of the amino acid sequences of MutT-related enzymes suggests that the enzymes with higher substrate specificity for 8-oxoG are only MutT homologs from closely related species with conserved amino acids in the positions that participate in the recognition of 8-oxoG and the conformational change (Fig. 1, *green asterisk*). In fact, these amino acids are not highly conserved among *E. coli* Orf135 (51), *Bacillus subtilis* YtkD (52), and hMTH1 (8) that have broad substrate specificities.

Structure of the MutT Signature and Metal-binding Sites—We have solved two types of Mn²⁺-bound structures, MutT-8-oxo-dGMP-Mn²⁺ and MutT-Mn²⁺, to determine metal-binding sites at the MutT signature of MutT. The crystal of MutT-Mn²⁺ contains two proteins per asymmetric unit. Their overall structures are very similar, with an r.m.s.d. of 0.3 Å for the corresponding 118 Cα atoms; for simplicity, only one molecule will be referred to in all further discussion. The structure of MutT-Mn²⁺ is similar to that of the apo form, with an r.m.s.d. of 0.6 Å for the corresponding 118 Cα atoms.

In the MutT signature having an SLHL structure (Fig. 4A), Gly-38, Glu-44, Arg-52, Glu-53, Glu-56, Glu-57, and Gly-59 are completely conserved among the members of the Nudix family (Fig. 1). The SLHL structure of MutT is similar to those of other enzymes in the Nudix family. For example, the conserved 23 residues can be superimposed on those found in the *Pyrobaculum aerophilum* Nudix protein with an r.m.s.d. of 0.5 Å (53). A characteristic feature in the SLHL structure is the hydrogen-bonding network centering on the converged Arg-52 that anchors α-1 to its connecting loop. The side chains of Glu-44 and Arg-52, which form two hydrogen bonds with each other, participate in hydrogen bonding to the main chain atoms in the nonconserved Glu-41 and Lys-39 residues, respectively. Arg-52 also interacts with the side chains of the conserved Glu-53 and Glu-56 residues (Fig. 4A). This hydrogen-bonding network is roughly the same as that in the other Nudix proteins and contributes to the conformational stability of the SLHL structure (39, 40, 53–65).

In the electron density maps of the MutT-Mn^{2+} crystal produced by co-crystallization, there were three peaks corresponding to the metal ions near the MutT signature. Judging from the peak heights, B factors, bond lengths, and bond angles, we determined that two peaks were Mn^{2+} ions (nearly ideal octahedral coordination and an average bond length of ~2.2 Å) and one was Na^+ (distorted octahedral coordination and an average bond length of ~2.5 Å) (Fig. 4B). Furthermore, the two Mn^{2+} sites were also confirmed from significant densities (>10 σ level) on the anomalous difference Fourier map at $\lambda = 1$ Å (data not shown). On the other hand, the densities of the Na^+ site were less than noise level. The refined MutT-Mn^{2+} structure reveals that two Mn^{2+} ions form a binuclear metal center with a bridged water molecule. One Mn^{2+} coordinates to the oxygen atoms of Glu-53, Glu-57, three water molecules, and Asp-77 in another molecule (Asp-77*). The coordination partners of another Mn^{2+} are Glu-53, L-tartrate (a crystallization reagent), and four water molecules. Na^+ coordinates to the oxygen atoms of Gly-37, Glu-57, Asp-77*, and two water molecules. Asp-77* and L-tartrate bind to the MutT signature through metal ions, but do not distort the SLHL structure.

In the MutT-8-oxo-dGMP-Mn^{2+} crystal (prepared by soaking MutT-8-oxo-dGMP crystals in reservoir supplemented with 1 mM $MnCl_2$), Mn^{2+} binds to the six oxygen atoms of the main chain of Gly-37, the side chain of Glu-57, the phosphate group, and three water molecules with nearly ideal octahedral coordination (Fig. 4A). The binding of Mn^{2+} to the MutT-8-oxo-dGMP binary complex makes the phosphate group move slightly toward Mn^{2+} (the P atom moves by 0.7 Å). The position of Mn^{2+} observed in MutT-8-oxo-dGMP-Mn^{2+} is close to that of Na^+ in MutT-Mn^{2+} (at a distance of 1.4 Å). The three Mn^{2+} binding sites consisting of the Mn^{2+} in MutT-8-oxo-dGMP-Mn^{2+} and two additional Mn^{2+} ions in MutT-Mn^{2+} (Fig. 4C) are located at common metal-binding sites observed in the Nudix family (60) and correspond to those observed in the ternary complexes of *E. coli* ADP-ribose pyrophosphatase, *Mycobacterium tuberculosis* ADP-ribose pyrophosphatase, *Caenorhabditis elegans* diadenosine $5',5'''-P^1,P^4$-tetraphosphate pyrophosphohydrolase, *Xenopus laevis* X29, human NUDT5, *Thermus thermophilus* Ndx2, and BdRppH (40, 55, 57, 64–67). Thus, the three sites are considered to be candidates for metal binding in 8-oxo-dGTP hydrolysis. Previous kinetic studies have shown that MutT binds to one Mn^{2+} in the absence of nucleotides and two Mn^{2+} ions in the presence of a nonspecific substrate analog, AMPCPP (68). The middle Mn^{2+} (*Mn2* in Fig. 4C) may be prebound to the active site, judging from the number of coordination partners in MutT and the Mn^{2+} ion (*Mn1* in Fig. 4C) found in MutT-8-oxo-dGMP-Mn^{2+}; otherwise, it and other Mn^{2+} ion (*Mn1* and *Mn3*, respectively in Fig. 4C) would be recruited with the substrate. The probability of the three metals binding to MutT in the presence of the real substrate 8-oxo-dGTP cannot be neglected because of the fact that the number of binding metals depends on the kinds of substrate analogs (40, 54, 60, 61, 64–66).

The structures of MutT-8-oxo-dGMP-Mn^{2+} and MutT-Mn^{2+} suggest structural insights into some essential or important residues for the 8-oxo-dGTP hydrolysis. Glu-53 and Glu-57 are essential for the suppression of spontaneous A:T to

C:G transversion mutations (69), and E53Q and E57Q mutants decrease k_{cat} by 10^4 to 10^5-fold (70). On the other hand, Glu-56 is nonessential for the suppression of the mutations (69), and E56Q and E98Q mutants have relatively small effects (<24-fold) on k_{cat} (70). These results agree with our structural studies showing that essential residues, Glu-53 and Glu-57, directly bind to metal ions, whereas important residues, Glu-56 and Glu98, make water-mediated interactions with metal ions (Fig. 4, A and B). Gly-37 and Gly-38, which are located at the surface of the ligand-binding site, are also revealed to be essential residues for the suppression of the mutations (69). The side chains of any residues except Gly in positions 37 and 38 would contact the base moiety of the nucleotide ligand and the essential residue for the catalysis, Glu-53, respectively (Fig. 4, A and C). For this reason, to express 8-oxo-dGTPase activity, residues 37 and 38 must be Gly, which has the smallest side chain.

A number of kinetic, mutational, and NMR studies of MutT using dGTP and/or a substrate analog, AMPCPP, have been reported, and a catalytic mechanism is proposed by Mildvan and coworkers (71). Compared with our structural data, there appear to be some differences in the metal-binding sites. Gly-38 is involved in metal coordination in their model, but Gly-37, instead of Gly-38, is a metal ligand in the structure of MutT-8-oxo-dGMP-Mn^{2+} (Fig. 4, A and C). The all-crystal structures of Nudix proteins show that the carbonyl oxygen of the corresponding residue to Gly-38 participates in the formation of β-sheet, whereas that of Gly-37 binds to a metal ion (40, 55, 57–59, 61, 64–67). Glu-56 and Glu98, which are metal ligands in the model proposed by Mildvan and coworkers, interact with water molecules bound to metal ions in our structures. The metal coordination scheme changes in the active site during the reaction, and a more proper enzymatic mechanism activated by metal ions might be examined by kinetic protein crystallography.

REFERENCES

1. Maki, H., and Sekiguchi, M. (1992) *Nature* **355**, 273–275
2. Taddei, F., Hayakawa, H., Bouton, M., Cirinesi, A., Matic, I., Sekiguchi, M., and Radman, M. (1997) *Science* **278**, 128–130
3. Au, K. G., Cabrera, M., Miller, J. H., and Modrich, P. (1988) *Proc. Natl. Acad. Sci. U.S.A.* **85**, 9163–9166
4. Cabrera, M., Nghiem, Y., and Miller, J. H. (1988) *J. Bacteriol.* **170**, 5405–5407
5. Michaels, M. L., Cruz, C., Grollman, A. P., and Miller, J. H. (1992) *Proc. Natl. Acad. Sci. U.S.A.* **89**, 7022–7025
6. Tchou, J., Kasai, H., Shibutani, S., Chung, M. H., Laval, J., Grollman, A. P., and Nishimura, S. (1991) *Proc. Natl. Acad. Sci. U.S.A.* **88**, 4690–4694
7. Ito, R., Hayakawa, H., Sekiguchi, M., and Ishibashi, T. (2005) *Biochemistry* **44**, 6670–6674
8. Fujikawa, K., Kamiya, H., Yakushiji, H., Fujii, Y., Nakabeppu, Y., and Kasai, H. (1999) *J. Biol. Chem.* **274**, 18201–18205
9. Fujikawa, K., Kamiya, H., Yakushiji, H., Nakabeppu, Y., and Kasai, H. (2001) *Nucleic Acids Res.* **29**, 449–454
10. Mishima, M., Sakai, Y., Itoh, N., Kamiya, H., Furuichi, M., Takahashi, M., Yamagata, Y., Iwai, S., Nakabeppu, Y., and Shirakawa, M. (2004) *J. Biol. Chem.* **279**, 33806–33815
11. Tchou, J., Bodepudi, V., Shibutani, S., Antoshechkin, I., Miller, J., Grollman, A. P., and Johnson, F. (1994) *J. Biol. Chem.* **269**, 15318–15324
12. Hatahet, Z., Kow, Y. W., Purmal, A. A., Cunningham, R. P., and Wallace, S. S. (1994) *J. Biol. Chem.* **269**, 18814–18820
13. Fromme, J. C., and Verdine, G. L. (2003) *J. Biol. Chem.* **278**, 51543–51548
14. Porello, S. L., Leyes, A. E., and David, S. S. (1998) *Biochemistry* **37**,

14756–14764

15. Bruner, S. D., Norman, D. P., and Verdine, G. L. (2000) *Nature* **403,** 859–866

16. Fromme, J. C., Banerjee, A., Huang, S. J., and Verdine, G. L. (2004) *Nature* **427,** 652–656

17. Bessman, M. J., Frick, D. N., and O'Handley, S. F. (1996) *J. Biol. Chem.* **271,** 25059–25062

18. Abeygunawardana, C., Weber, D. J., Gittis, A. G., Frick, D. N., Lin, J., Miller, A. F., Bessman, M. J., and Mildvan, A. S. (1995) *Biochemistry* **34,** 14997–15005

19. Massiah, M. A., Saraswat, V., Azurmendi, H. F., and Mildvan, A. S. (2003) *Biochemistry* **42,** 10140–10154

20. Doublié, S. (1997) *Methods Enzymol.* **276,** 523–530

21. LeMaster, D. M., and Richards, F. M. (1985) *Biochemistry* **24,** 7263–7268

22. Nakamura, T., Kitaguchi, Y., Miyazawa, M., Kamiya, H., Toma, S., Ikemizu, S., Shirakawa, M., Nakabeppu, Y., and Yamagata, Y. (2006) *Acta Crystallogr. Sect. F Struct. Biol. Cryst. Commun.* **62,** 1283–1285

23. Akiyama, M., Maki, H., Sekiguchi, M., and Horiuchi, T. (1989) *Proc. Natl. Acad. Sci. U.S.A.* **86,** 3949–3952

24. Nakamura, T., Doi, T., Sekiguchi, M., and Yamagata, Y. (2004) *Acta Crystallogr. D Biol. Crystallogr.* **60,** 1641–1643

25. Rossmann, M. G., and van Beek, C. G. (1999) *Acta Crystallogr. D Biol. Crystallogr.* **55,** 1631–1640

26. Otwinowski, Z., and Minor, W. (1997) *Methods Enzymol.* **276,** 307–326

27. Matthews, B. W. (1968) *J. Mol. Biol.* **33,** 491–497

28. Terwilliger, T. C., and Berendzen, J. (1999) *Acta Crystallogr. D Biol. Crystallogr.* **55,** 849–861

29. Collaborative Computational Project, Number 4. (1994) *Acta Crystallogr. D Biol. Crystallogr.* **50,** 760–763

30. Cowtan, K. (1994) *Joint CCP4 and ESF-EACBM Newsletter on Protein Crystallography* **31,** 34–38

31. Cambillau, C., Horjales, E., and Jones, T. A. (1984) *J. Mol. Graph.* **2,** 53–54

32. Jones, T. A., Zou, J. Y., Cowan, S. W., and Kjeldgaard, M. (1991) *Acta Crystallogr. Sect. A* **47,** 110–119

33. Brünger, A. T. (1992) *A System for X-Ray Crystallography and NMR,* Yale University Press, New Haven, CT

34. Brünger, A. T., Adams, P. D., Clore, G. M., DeLano, W. L., Gros, P., Grosse-Kunstleve, R. W., Jiang, J. S., Kuszewski, J., Nilges, M., Pannu, N. S., Read, R. J., Rice, L. M., Simonson, T., and Warren, G. L. (1998) *Acta Crystallogr. D Biol. Crystallogr.* **54,** 905–921

35. Navaza, J. (1994) *Acta Crystallogr. Sect. A* **50,** 157–163

36. Laskowski, R. A., MacArthur, M. W., Moss, D. S., and Thornton, J. M. (1993) *J. Appl. Crystallogr.* **26,** 283–291

37. Kabsch, W. (1976) *Acta Crystallogr. Sect. A* **32,** 922–923

38. DeLano, W. L. (2002) *The PyMOL Molecular Graphics System,* DeLano Scientific LLC, San Carlos, CA

39. Gabelli, S. B., Bianchet, M. A., Xu, W., Dunn, C. A., Niu, Z. D., Amzel, L. M., and Bessman, M. J. (2007) *Structure* **15,** 1014–1022

40. Messing, S. A., Gabelli, S. B., Liu, Q., Celesnik, H., Belasco, J. G., Piñeiro, S. A., and Amzel, L. M. (2009) *Structure* **17,** 472–481

41. Holm, L., Kääriäinen, S., Rosenström, P., and Schenkel, A. (2008) *Bioinformatics* **24,** 2780–2781

42. Bhatnagar, S. K., Bullions, L. C., and Bessman, M. J. (1991) *J. Biol. Chem.* **266,** 9050–9054

43. Saenger, W. (1984) *Principles of Nucleic Acid Structure,* Springer-Verlag, New York

44. Steyert, S. R., Messing, S. A., Amzel, L. M., Gabelli, S. B., and Piñeiro, S. A. (2008) *J. Bacteriol.* **190,** 8215–8219

45. Saraswat, V., Massiah, M. A., Lopez, G., Amzel, L. M., and Mildvan, A. S. (2002) *Biochemistry* **41,** 15566–15577

46. Saraswat, V., Azurmendi, H. F., and Mildvan, A. S. (2004) *Biochemistry* **43,** 3404–3414

47. Funahashi, J., Takano, K., Yamagata, Y., and Yutani, K. (2002) *J. Biol. Chem.* **277,** 21792–21800

48. Takano, K., Yamagata, Y., Funahashi, J., Hioki, Y., Kuramitsu, S., and Yutani, K. (1999) *Biochemistry* **38,** 12698–12708

49. Kouchakdjian, M., Bodepudi, V., Shibutani, S., Eisenberg, M., Johnson, F., Grollman, A. P., and Patel, D. J. (1991) *Biochemistry* **30,** 1403–1412

50. Uesugi, S., Yano, J., Yano, E., and Ikehara, M. (1977) *J. Am. Chem. Soc.* **99,** 2313–2323

51. Kamiya, H., Murata-Kamiya, N., Iida, E., and Harashima, H. (2001) *Biochem. Biophys. Res. Commun.* **288,** 499–502

52. Xu, W., Jones, C. R., Dunn, C. A., and Bessman, M. J. (2004) *J. Bacteriol.* **186,** 8380–8384

53. Wang, S., Mura, C., Sawaya, M. R., Cascio, D., and Eisenberg, D. (2002) *Acta Crystallogr. D Biol. Crystallogr.* **58,** 571–578

54. Gabelli, S. B., Bianchet, M. A., Bessman, M. J., and Amzel, L. M. (2001) *Nat. Struct. Biol.* **8,** 467–472

55. Bailey, S., Sedelnikova, S. E., Blackburn, G. M., Abdelghany, H. M., Baker, P. J., McLennan, A. G., and Rafferty, J. B. (2002) *Structure* **10,** 589–600

56. Kang, L. W., Gabelli, S. B., Bianchet, M. A., Xu, W. L., Bessman, M. J., and Amzel, L. M. (2003) *J. Bacteriol.* **185,** 4110–4118

57. Kang, L. W., Gabelli, S. B., Cunningham, J. E., O'Handley, S. F., and Amzel, L. M. (2003) *Structure* **11,** 1015–1023

58. Shen, B. W., Perraud, A. L., Scharenberg, A., and Stoddard, B. L. (2003) *J. Mol. Biol.* **332,** 385–398

59. Gabelli, S. B., Bianchet, M. A., Azurmendi, H. F., Xia, Z., Sarawat, V., Mildvan, A. S., and Amzel, L. M. (2004) *Structure* **12,** 927–935

60. Ranatunga, W., Hill, E. E., Mooster, J. L., Holbrook, E. L., Schulze-Gahmen, U., Xu, W., Bessman, M. J., Brenner, S. E., and Holbrook, S. R. (2004) *J. Mol. Biol.* **339,** 103–116

61. Yoshiba, S., Ooga, T., Nakagawa, N., Shibata, T., Inoue, Y., Yokoyama, S., Kuramitsu, S., and Masui, R. (2004) *J. Biol. Chem.* **279,** 37163–37174

62. She, M., Decker, C. J., Chen, N., Tumati, S., Parker, R., and Song, H. (2006) *Nat. Struct. Mol. Biol.* **13,** 63–70

63. Zha, M., Zhong, C., Peng, Y., Hu, H., and Ding, J. (2006) *J. Mol. Biol.* **364,** 1021–1033

64. Scarsdale, J. N., Peculis, B. A., and Wright, H. T. (2006) *Structure* **14,** 331–343

65. Wakamatsu, T., Nakagawa, N., Kuramitsu, S., and Masui, R. (2008) *J. Bacteriol.* **190,** 1108–1117

66. Gabelli, S. B., Bianchet, M. A., Ohnishi, Y., Ichikawa, Y., Bessman, M. J., and Amzel, L. M. (2002) *Biochemistry* **41,** 9279–9285

67. Zha, M., Guo, Q., Zhang, Y., Yu, B., Ou, Y., Zhong, C., and Ding, J. (2008) *J. Mol. Biol.* **379,** 568–578

68. Frick, D. N., Weber, D. J., Gillespie, J. R., Bessman, M. J., and Mildvan, A. S. (1994) *J. Biol. Chem.* **269,** 1794–1803

69. Shimokawa, H., Fujii, Y., Furuichi, M., Sekiguchi, M., and Nakabeppu, Y. (2000) *Nucleic Acids Res.* **28,** 3240–3249

70. Harris, T. K., Wu, G., Massiah, M. A., and Mildvan, A. S. (2000) *Biochemistry* **39,** 1655–1674

71. Mildvan, A. S., Xia, Z., Azurmendi, H. F., Saraswat, V., Legler, P. M., Massiah, M. A., Gabelli, S. B., Bianchet, M. A., Kang, L. W., and Amzel, L. M. (2005) *Arch. Biochem. Biophys.* **433,** 129–143

72. Thompson, J. D., Higgins, D. G., and Gibson, T. J. (1994) *Nucleic Acids Res.* **22,** 4673–4680
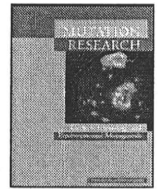
Phenylalanine 171 is a molecular brake for translesion synthesis across benzo[a]pyrene-guanine adducts by human DNA polymerase kappa

Akira Sassa[a,b], Naoko Niimi[a], Hirofumi Fujimoto[c], Atsushi Katafuchi[a], Petr Grúz[a], Manabu Yasui[a], Ramesh C. Gupta[d], Francis Johnson[d], Toshihiro Ohta[b], Takehiko Nohmi[a,*]

[a] Division of Genetics and Mutagenesis, National Institute of Health Sciences, 1-18-1 Kamiyoga, Setagaya-ku, Tokyo 158-8501, Japan
[b] School of Life Sciences, Tokyo University of Pharmacy and Life Sciences, Hachiouji-shi, Tokyo 192-0392, Japan
[c] Division of Radiological Protection and Biology, National Institute of Infectious Diseases, 1-23-1 Toyama, Shinjuku-ku, Tokyo 162-8640, Japan
[d] Department of Pharmacological Sciences, Stony Brook University, Stony Brook, New York 11794-3400, NY, United States

ARTICLE INFO

ABSTRACT

Human cells possess multiple specialized DNA polymerases (Pols) that bypass a variety of DNA lesions which otherwise would block chromosome replication. Human polymerase kappa (Pol κ) bypasses benzo[a]pyrene diolepoxide-N^2-deoxyguanine (BPDE-N^2-dG) DNA adducts in an almost error-free manner. To better understand the relationship between the structural features in the active site and lesion bypass by Pol κ, we mutated codons corresponding to amino acids appearing close to the adducts in the active site, and compared bypass efficiencies. Remarkably, the substitution of alanine for phenylalanine 171 (F171), an amino acid conserved between Pol κ and its bacterial counterpart *Escherichia coli* DinB, enhanced the efficiencies of dCMP incorporation opposite (−)- and (+)-trans-anti-BPDE-N^2-dG 18-fold. This substitution affected neither the fidelity of TLS nor the efficiency of dCMP incorporation opposite normal guanine. This amino acid change also enhanced the binding affinity of Pol κ to template/primer DNA containing (−)-trans-anti-BPDE-N^2-dG. These results suggest that F171 functions as a molecular brake for TLS across BPDE-N^2-dG by Pol κ and that the F171A derivative of Pol κ bypasses these DNA lesions more actively than does the wild-type enzyme.

© 2010 Elsevier B.V. All rights reserved.

1. Introduction

Human genomic DNA is continually subject to damage caused by exogenous and endogenous genotoxic agents. The progress of the replicative DNA polymerases (Pols), such as Pol α, Pol δ and Pol ε, can be blocked by DNA lesions, possibly leading to cell death. However, these blocks can be circumvented by translesion synthesis (TLS) catalyzed by specialized Pols, or by the recombination of damaged template DNA [1,2]. Human cells possess multiple specialized Pols, including Pol η, Pol ι, Pol κ, Rev1, and Pol ζ; Pol ζ is a member of the B family and the others are members of the Y family [3]. These Pols contribute to cell survival by inserting dNMPs opposite the lesions in template DNA in an error-free or error-prone manner, thus promoting continuous chromosome replication. An example of error-free TLS is the Pol η-dependent insertion of two dAMPs opposite a cis-syn thymine DNA dimer, protecting human skin cells from ultraviolet light-induced DNA damage. Pol η deficiency leads to the genetic disease Xeroderma pigmentosum variant, resulting in increased susceptibility to ultraviolet light-induced skin cancer [4,5]. However, Pol η is suggested to be involved in error-prone TLS via its incorporation of incorrect dNMPs opposite certain DNA lesions, for example, N^2-deoxyguanosine (dG) adducts derived from 2-amino-3-methylimidazo[4,5-f]quinoline [6]. Such erroneous TLS may result in mutagenesis, carcinogenesis, and perhaps aging [7–9]. Thus, TLS can be a double-edged sword, as the mechanisms contributing to genomic integrity in the face of genotoxic agents can themselves result in mutation.

Benzo[a]pyrene (BP) is a ubiquitous environmental pollutant that is present in tobacco smoke and is released to the air as a product of fossil fuel combustion [10]. Upon incorporation into cells (mainly through the lungs), BP is metabolised to various reactive intermediates, the most mutagenic and tumorigenic of which is benzo[a]pyrene-7,8-dihydrodiol-9,10-epoxide (BPDE) [10,11]. Pol

---

Abbreviations: Pol, DNA polymerase; TLS, translesion DNA synthesis; dG, N^2-deoxyguanosine; BP, benzo[a]pyrene; BPDE, benzo[a]pyrene-7,8-dihydrodiol-9,10-epoxide; (+)-BPDE-N^2-dG, (+)-trans-anti-BPDE-N^2-dG; (−)-BPDE-N^2-dG, (−)-trans-anti-BPDE-N^2-dG; F171, phenylalanine 171; R175, arginine 175; L197, leucine 197; F171A (R175AL197A, D198A or E199A), a variant of hPol κ having alanine instead of F171 (R175, L197, D198 or E199); PAGE, polyacrylamide gel electrophoresis; 18C (AT or G), Alexa546-labelled 18-mer standard DNA containing dC (A, T or G) at the 13th position; $17\Delta^1$, 17-mer DNA lacking one base at the 13th position; $16\Delta^2$, 16-mer DNA lacking two bases at positions 13 and 14; K_D, the equilibrium dissociation constant; D198, aspartic acid 198; E199, glutamic acid 199.

* Corresponding author. Tel.: +81 3 3700 9872; fax: +81 3 3700 2348.
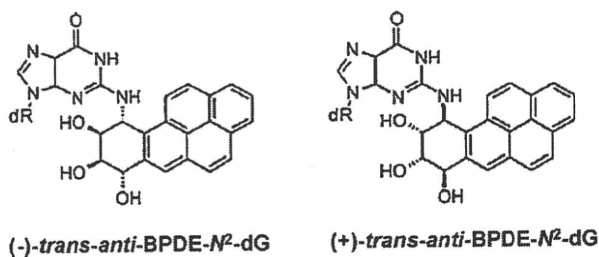 *E-mail address:* nohmi@nihs.go.jp (T. Nohmi).

Fig. 1. Structures of the (−)- and (+)-BPDE-dG adducts.

(−)-*trans-anti*-BPDE-*N²*-dG   (+)-*trans-anti*-BPDE-*N²*-dG

κ, a homologue of *Escherichia coli* DinB (DNA Pol IV), appears to be involved in error-free TLS across N^2-deoxyguanine adducts induced by BPDE, specifically (+)- and (−)-trans-anti-BPDE-N^2-dG (Fig. 1)(hereafter, we call them (+)-BPDE-dG and (−)-BPDE-dG, respectively). Pol κ strongly binds to DNA containing (−)-BPDE-dG [12], and preferentially incorporates dCMP opposite both (+) and (−) lesions [12–17]. Pol κ has been implicated in error-free TLS past (+)-BPDE-dG in mouse embryonic fibroblasts transfected with a gapped plasmid containing a site-specific lesion [18]. Embryonic fibroblasts from Pol $\kappa^{-/-}$ mice display sensitivity to the killing effects of racemic (±)-anti-BPDE, as well as the mutagenic and killing effects of BP plus rat liver homogenates (S9 enzymes) in the presence of caffeine [19,20]. However, the catalytic mechanism by which Pol κ bypasses across (+)- and (−)-BPDE-dG is not fully understood.

Fortunately, X-ray structures of the ternary complex of Pol κ with DNA and incoming dNTPs have been resolved [21]. Based on these structures, it has been suggested that N^2-dG adducts, for example trans-4-hydroxy-2-nonenal-N^2-dG, are positioned at the minor groove in the active site. The predicted amino acid residues proximal to the adducts are phenylalanine 171 (F171), arginine 175 (R175), and leucine 197 (L197). Molecular dynamics studies also suggest that F171, which is conserved between Pol κ and *E. coli* DinB, stacks with the pyrene ring of (+)-BPDE-dG [22]. The goal of the current study is to elucidate the relationship between these Pol κ structural features and the TLS process. We have changed F171, R175, or L197 to alanine, and examined the TLS activities and DNA binding properties of the resulting mutant Pols. Remarkably, the substitution of F171 to alanine increased the TLS activities approximately 18-fold, and significantly enhanced the ability to bind DNA with (−)-BPDE-dG. These results suggest that the conserved F171 acts a molecular brake for Pol κ-mediated TLS across the BP adducts; additional space to accommodate the bulky lesions in the active site may be required for active TLS. Because of the presence of the molecular brake in the active site, we speculate that Pol κ may not have evolved to bypass the BPDE adducts or perhaps other adducts induced by polycyclic aromatic hydrocarbons. Possible candidates for DNA lesions suitable for TLS by Pol κ are discussed.

2. Materials and methods

2.1. Proteins

Human wild-type Pol κ and variant proteins with alanine substitutions (F171A, R175A, L197A) were prepared as C-terminal truncations with 10 His-tags, including 559 N-terminal residues as previously described [12]. Briefly, overexpression plasmids for F171A, R175A, and L197A were constructed from pYG8591 by site-directed mutagenesis using PCR. pYG8591 was also used for overexpression of wild-type Pol κ. The resulting plasmids were transformed into Rosetta (DE3) pLysS (Novagen), and protein expression was induced with isopropyl β-D-1-thiogalactopyranoside. Wild-type Pol κ, F171A, R175A and L197A were purified to near homogeneity using BD TALON Metal Affinity Resins (BD Biosciences), gel filtration (16/60 Superdex 200 pg, GE Healthcare), and ion-exchange chromatography (HiTrap Heparin HP columns, GE Healthcare) with an FPLC system (AKTAexplorer 10 s, GE Healthcare) (Fig. 1 of the Supporting Information).
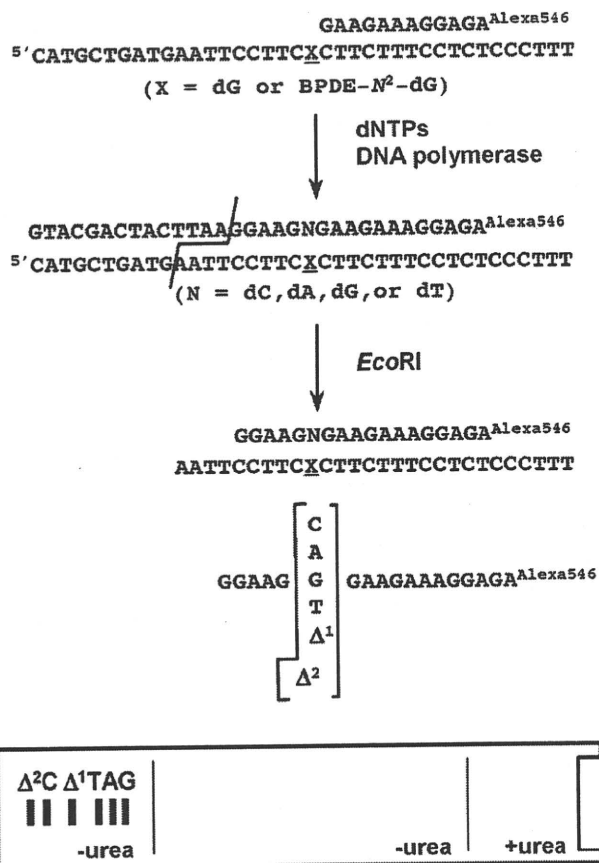

Fig. 2. Fluorescent two-phase PAGE determines miscoding specificity of DNA adducts. Unmodified and (−)-/(+)-BPDE-dG-modified 38-mer templates were annealed to Alexa546-labelled 12-mer primers. Primer extension reactions catalyzed by wild-type or F171A Pol κ were conducted in the presence of all four dNTPs at concentration of 100 μM each. Fully-extended products formed during DNA synthesis were recovered from the 20% polyacrylamide gel, annealed with a complementary 38-mer, cleaved with *EcoRI*, and subjected to two-phase PAGE (Section 2). To determine miscoding specificities, mobilities of the reaction products were compared with those of 18-mer standards containing dC, dA, dG, or dT opposite the lesion, and one-base (Δ^1) or two-base (Δ^2) deletions.

2.2. Oligonucleotide preparation

5′-Cy3-labelled oligonucleotides used for primers were purchased from BEX Co., Ltd. (Tokyo, Japan). Oligonucleotides labelled with biotin or Alexa546 at the 5′ end, unmodified template oligonucleotides, and oligonucleotides with thymine glycol were purchased from Japan Bio Services Co., Ltd. (Saitama, Japan). Oligonucleotides containing (−)- or (+)-BPDE-dG were synthesized as previously reported [23].

2.3. TLS assays

The Cy3-labelled primer DNA (5′-CTTCCCTAGGAATT-3′) was annealed to the template DNA (5′-GCGCGCTTCTGGCCAAT X̲GCAGAATTCCTAGGGAAG-3′, where X̲ represents dG, (−)-BPDE-dG, or (+)-BPDE-dG) at a molar ratio of 1:1.2. 100 nM primer/template DNA hybrid was incubated with 1, 5, or 20 nM wild-type or mutant Pol κ in 10 μL reaction mixtures containing 40 mM Tris–HCl (pH 8.0), 5 mM MgCl$_2$, 10 mM DTT, 0.1 mg/mL BSA, 60 mM KCl, 2.5% glycerol, and 100 μM each of the four dNTPs. The reactions were carried out for 1 min or 10 min at 37 °C, and were terminated by addition of termination buffer (98% formamide, 10 mM EDTA, 10 mg/mL blue dextran). After heat denaturation at 95 °C for 5 min, the products were separated by 15% polyacrylamide gel electrophoresis (PAGE) on gels containing 8 M urea. The separated products were visualized with the Molecular Imager FX Pro System (Bio-Rad Laboratories) and quantified with Quantity One software version 4.5 (Bio-Rad Laboratories).

2.4. Steady-state kinetics analyses

When measuring the kinetic parameters for nucleotide insertion opposite dG, (−)-BPDE-dG, (+)-BPDE-dG, or thymine glycol, the reaction mixtures were identical

to the TLS assay mixtures except for the addition of 3–5 nM wild-type or variant Pol κ and varying amounts of single dNTPs. The 36-mer template DNA, containing thymine glycol and annealed to the 18-mer primer DNA, was also used for the steady-state kinetic assay. For incorporation kinetics opposite dG, reaction mixtures containing dCTP (0.2–20 μM) and 3 nM wild-type or variant Pol κ were incubated for 30 s. For incorporation kinetics opposite (−)-BPDE-dG, reaction mixtures containing dCTP (50–4000 μM) and 3 nM wild-type or variant Pol κ were incubated for 3 min (wild-type or R175A), 30 s (F171A) or 5 min (L197A). For incorporation kinetics opposite (+)-BPDE-dG, reaction mixtures containing dCTP (20–1000 μM) and 5 nM wild-type or variant Pol κ were incubated for 20 min (wild-type, R175A or L197A) or 3 min (F171A). For incorporation kinetics opposite thymine glycol, reaction mixtures containing dATP (20–1000 μM) and 3 nM wild-type or variant Pol κ were incubated for 30 s. To measure the extension parameters, the reaction mixtures were identical to the nucleotide insertion reactions, except that 120 nM Cy3-labelled 19-mer primer (5′-CTTCCCTAGGAATTCTGCC-3′) replaced the 18-mer primer. The concentrations of dNTPs and the incubation times were varied according to the activity of given Pols. For extension kinetics from dG/dC, reaction mixtures containing dATP (0.2–20 μM) and 3 nM wild-type or variant Pol κ were incubated for 30 s. For extension kinetics from (−)-BPDE-dG/dC, reaction mixtures containing dATP (2–200 μM) and 3 nM wild-type or variant Pol κ were incubated for 30 s (wild-type, R175A and L197A) or 20 s (F171A). For extension kinetics from (+)-BPDE-dG/dC, reaction mixtures containing dATP (2–200 μM) and 3 nM wild-type or variant Pol κ were incubated for 10 min (wild-type, R175A and L197A) or 3 min (F171A). For extension kinetics from thymine glycol/dA, reaction mixtures containing dATP (20–500 μM) and 3 nM wild-type or variant Pol κ were incubated for 30 s. The products were analyzed as described for TLS assays. The rate of incorporation was plotted against dNTP concentrations, and the apparent Michaelis–Menten constants, K_m, and V_{max} values were determined by the Enzyme Kinetics Module 1.1 of SigmaPlot 2001 software version 7.101 (SPSS, Inc). k_{cat} was calculated by dividing the V_{max} by the enzyme concentration. All values represent means plus standard errors from three independent experiments.

2.5. Quantitative assays for miscoding specificity

The method used to determine miscoding specificities has been previously described [24–26] and is presented in Fig. 2. Briefly, 5′-Alexa546-labelled 12-mer primer (5′-AGAGGAAAGAAG-3′) was annealed to 38-mer template DNA (5′-CATGCTGATGAATTCCTTCXCTTCTTTCCTCTCCCTTT-3′), where X represents dG, (−)-BPDE-dG, or (+)-BPDE-dG) at a 1:1.5 ratio. 50 nM primer/template DNA was incubated with 2.5 nM wild-type Pol κ or F171A for 30 min at 25 °C in the presence of all four dNTPs (100 μM).

Approximately 80% of primer DNA was converted to full length to ensure that the assay has an ability to detect infrequent occurrences. Namely, 81.2%, 76.8% and 80.9% of the starting primer DNA was fully extended when the wild-type Pol κ continued DNA synthesis across dG, (−)-BPDE-dG and (+)-BPDE-dG, respectively. Similarly, 83.8%, 78.5% and 79.5% of the starting primer DNA was converted to the fully-extended products when F171A continued DNA synthesis across dG, (−)-BPDE-dG and (+)-BPDE-dG, respectively. The extended products were separated by 20% denaturing PAGE and extracted from the gel. The extracted DNA was annealed to the unmodified 38-mer template having dG at the position X, cleaved with EcoRI, and subjected to two-phase PAGE with 7 M urea in the upper phase and no urea in the lower phase. To determine base substitutions and deletions, we used Alexa546-labelled 18-mer standard DNA containing dC, dA, dG, or dT at the 13th position (18C, 18A, 18G or 18T, respectively, shown in Fig. 4), 17-mer DNA lacking one base at the 13th position ($17\Delta^1$), or 16-mer DNA lacking two bases at positions 13 and 14 ($16\Delta^2$) as authentic samples for comparison with reaction product mobility [25,26]. Exact sequences of the authentic samples are shown in Fig. 2. The separated products were visualized with the Molecular Imager FX Pro System (Bio-Rad Laboratories) and quantified with Quantity One software version 4.5 (Bio-Rad Laboratories).

2.6. DNA binding BIAcore assay

The DNA binding assay was performed using the BIAcore3000 instrument (GE Healthcare) as previously described [12]. Oligonucleotides were similar to those used in the primer extension assay, except for 5′-biotinylation of the primers for immobilisation to the Sensor Chip SA (GE Healthcare). The equilibrium dissociation constants (K_D) were calculated from the kinetic traces using BIAevaluation version 4.0, employing local fitting according to the "1:1 binding with drifting baseline" predefined model (GE Healthcare).

2.7. Modeling of (−)- and (+)-BPDE-adducts in the Pol κ active site

To visualize the relative positions of F171/A171 and (−)-/(+)-BPDE-dG following the incorporation of dCMP opposite (−)-/(+)-BPDE-dG, the conformation of (−)-/(+)-BPDE-dG with dCTP in the active site of Pol κ was drawn based on the reported crystallographic structure of Pol κ with DNA and incoming dTTP [PDB ID: 2OH2 [21]], using the 2007.09 version of the Molecular Operating Environment (MOE) (Chemical Computing Group Inc., Montreal, Canada) and MOE-ASEDock 2005 [27]. We replaced the original dTTP with dCTP, and substituted the original template dA with (−)-BPDE-dG [PDB ID: 1AXL [28]] or (+)-BPDE-dG [PDB ID: 1AXO [29]].

The resulting template and primer sequences were 5′-CCXGGGTCCTTCCCC-3′ and 5′-GGGGAAGGACCC-3′, respectively, where X represents (−)-BPDE-dG or (+)-BPDE-dG. After all replacements, we minimised the potential energies of F171 and the replaced residues. The F171A mutant was visualized by substituting alanine for F171 and repeating the above processes.

3. Results

3.1. Enhanced incorporation of dCMP opposite (−)- and (+)-BPDE-adducts by F171A

Primer extension reactions were performed in order to examine the effects of alanine substitutions of residues F171, R175, and L197 on the translesion activities of Pol κ variants (Fig. 3). Interestingly, TLS by F171A past (−)- and (+)-BPDE-dGs was much more active than by wild-type Pol κ. DNA synthesis by F171A past unmodified dG appeared similar to that of the wild-type enzyme (Fig. 3A). DNA synthesis by R175A and L197A across unmodified dG, the (−)- or (+)-BP lesions was lower than that of the wild-type Pol κ.

As a quantitative analysis, we carried out steady-state kinetic analyses to determine the catalytic efficiencies (k_{cat}/K_m) of dCMP incorporation opposite unmodified dG, dCMP incorporation opposite the BP lesions, and dAMP opposite thymine glycol (Fig. 2 of the Supporting Information and Table 1). Remarkably, the efficiency of dCMP incorporation opposite (−)- and (+)-BPDE-dGs by F171A was 18-fold higher than by the wild-type Pol κ, while the k_{cat}/K_m values for dCMP incorporation opposite normal dG were almost identical. Both Pols bypassed the (−)-adduct approximately four times more actively than the (+)-adduct. In contrast, the efficiency of dATP incorporation opposite thymine glycol by F171A was less than two-fold higher than by the wild-type Pol κ. Therefore, the marked increase in catalytic efficiency by the amino acid substitution appeared specific to TLS across the BPDE-adducts. The incorporation efficiencies displayed by the R175A variant were the same as the wild-type Pol κ. Finally, the substitution of L197 to alanine reduced efficiency by 30% for incorporation opposite the BPDE-adducts, and by 50% for incorporation opposite thymine glycol.

We also determined the kinetic parameters for extension reactions; the k_{cat} and K_m values for dAMP incorporation opposite template dT next to unmodified dG or the lesions appear in Table 1. Extension of 3′-dC primers was enhanced 1.6-fold and 3.7-fold opposite template (−)- and (+)-BPDE-dGs, respectively, by F171A Pol κ relative to wild type. The extension efficiency of F171A from 3′-dA opposite thymine glycol was 1.3-fold higher than by the wild type. Thus it would appear that the F171A substitution affects the extension reactions less than the insertion reactions. The extension efficiencies of R175A and L197A from dCs opposite (−)- and (+)-BPDE-dGs and from dA opposite thymine glycol were the same or lower in comparison to the wild-type enzyme. We also prepared and purified a catalytically "dead" variant of Pol κ, in which the active-site residues aspartic acid 198 (D198) and glutamic acid 199 (E199) were substituted with alanine (D198A/E199A), by the same method as for F171A, R195A and L197A. D198A/E199A Pol κ completely lost polymerase activity (data not shown). Therefore, the possibility that bacterial polymerases, such as DNA polymerase IV (DinB), may have contaminated the preparations of F171A, R195A and L197A and affected the results can be ruled out.

3.2. Comparison of DNA synthesis fidelities of wild-type and F171A Pol κ across (−)- and (+)-BPDE-adducts

We wished to determine whether the TLS enhancement displayed by the F171A variant was accompanied by an increased mutation (substitutions and deletions) rate of sequences containing BP lesions. Examination of the molecules produced by wild-type